ELSEVIER

### Contents lists available at ScienceDirect

# Ocean Modelling

journal homepage: www.elsevier.com/locate/ocemod



# Subgrid theory for storm surge modeling

Andrew B. Kennedy <sup>a,\*</sup>, Damrongsak Wirasaet <sup>a</sup>, Amirhosein Begmohammadi <sup>a</sup>, Thomas Sherman <sup>a</sup>, Diogo Bolster <sup>a</sup>, J.C. Dietrich <sup>b</sup>



b Department of Civil, Construction, and Environmental Engineering, North Carolina State University, NC, 27695, USA



#### ARTICLE INFO

Keywords: Subgrid methods Storm surge Numerical methods Mathematical modeling Shallow water equations

#### ABSTRACT

Averaging techniques are used to generate upscaled forms of the shallow water equations for storm surge including subgrid corrections. These systems are structurally similar to the standard shallow water equations but have additional terms related to integral properties of the fine-scale bathymetry, topography, and flow. As the system only operates with coarse-scale variables (such as averaged fluid velocity) relating to flow, these fine-scale integrals require closures to relate them to the coarsened variables. Closures with different levels of complexity are identified and tested for accuracy against high resolution solutions of the standard shallow water equations. Results show that, for coarse grids in complex geometries, inclusion of subgrid closure terms greatly improves model accuracy when compared to standard solutions, and will thereby enable new classes of storm surge models.

## 1. Introduction

Modern storm surge models have been split into two disparate branches based on their intended uses:

- Low resolution ensemble forecasts: Using hundreds to thousands of surge model runs, these models are largely used before tropical cyclone landfalls or for climatological surge studies (Zachry et al., 2017). Each realization is typically run on a single computational core, and uses relatively coarse computational grids to ensure that they can finish the many runs required within tight forecast windows.
- High resolution simulations: These are either performed singly or in small ensembles in forecasts, or in potentially much larger quantity for hindcasts or climatological studies. Such simulations are almost invariably run on large parallel computing systems (Anon., 2015; Hope et al., 2013).

Differences between these two varieties of simulation are characterized by run times and accuracy: low resolution models are much faster but have generally lower accuracy and vice versa for high resolution models (Kerr et al., 2013).

This state of affairs has existed for at least the past decade, but neither camp is entirely satisfied: the low resolution modelers would like to increase accuracy, while the high resolution camp often cannot complete simulations in the times it desires, and also requires expensive computational hardware that is not readily available to many. Furthermore, extremely high resolution topographic and bathymetric datasets

are increasingly becoming available in many locations, with detail that cannot currently be resolved by *any* large scale surge models (Danielson et al., 2018).

An intermediate path exists with the use of subgrid models (Defina, 2000; Casulli, 2009; Casulli and Stelling, 2011; Volp et al., 2013). It is well known that quantities in high resolution models are not completely independent. For example, nearby surface elevations are very highly correlated, so knowledge at one location implies a good knowledge of surface elevations at nearby locations also, even if they lie on a different computational grid cell. Subgrid models make use of such correlations to strongly reduce the number of computational degrees of freedom while retaining their bulk effects in modified sets of equations.

The fundamental assumption of subgrid models, which is not often stated explicitly, is that subgrid effects are uniquely defined and can be adequately represented by functions of coarsened (averaged) properties, such as water levels or velocities, combined with integral functions of high resolution ground elevations, friction characteristics and so on. The accuracy of subgrid solutions depends greatly on these coarsened properties: for many cases, systems display strong correlations that enable the subgrid system to retain almost all of the accuracy of the original high-resolution system. In other cases, detailed subgrid properties may not be unique functions of coarsened properties: a simple example is shown in Fig. 1 where water levels on either side of a levee are independent quantities. In this case, one water level is insufficient to represent important details of the system because the two water bodies are not connected. However, if the water level were high

E-mail address: andrew.kennedy@nd.edu (A.B. Kennedy).

Corresponding author.

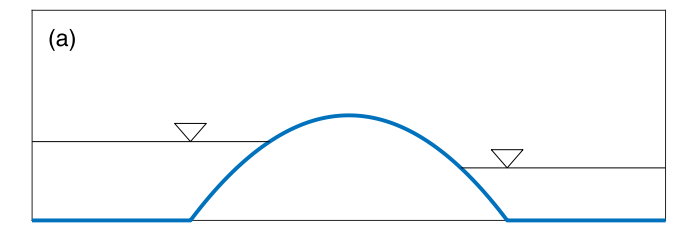
enough to inundate the levee, then a single variable to represent water levels would become much more viable. Some of these same tradeoffs are also present, usually unannounced and unevaluated, in standard storm surge models, where simple velocity, elevation, and bathymetry distributions within a cell are simply assumed to adequately represent the processes of interest.

The concept of subgrids is implicit in many aspects of hydrodynamics: as one example, Manning's equation used in channel flow hydraulics (Te Chow, 1982) explicitly constructs a solution with lower degrees of freedom from higher resolution bathymetry and land cover. Similarly, Darcy's law for porous media flow aggregates the effects of very small scale unresolved features into a coarser scale continuum. Importantly, it is possible to construct Darcy's law from first principles using subgrid physical properties of a porous medium (Whitaker, 1999), which is similar to our intention here.

Subgrids for surge/inundation/circulation modeling have been explored previously by several groups, but using somewhat different techniques than will be applied here. Defina (2000) developed a set of equations that looked much like the conservative form of the shallow water equations, but with a correction to the mass conservation equation that accounts for partially wet-partially dry regions, and separate corrections to momentum and bottom friction arising from non-uniform spatial velocities. The wet-dry fraction was assumed to have an errorfunction variation with surface elevation. Casulli (2009) developed an elegant theory/numerical technique for subgrid wetting and drying that guarantees non-negative depths at the shoreline through the solution of a mildly nonlinear equation. This system again closely resembles nonlinear shallow water equations with a correction for partially wet elements. In contrast to Defina's work, Casulli (2009) used lookup tables derived from high resolution bathymetry to obtain the wet fraction as a function of surface elevation. Sehili et al. (2014) implemented results from Casulli (2009) and Casulli and Stelling (2011) to examine storm surge flooding around Hamburg and found that the subgrid system delivered similar accuracy to the standard shallow water equations, but with around 5% of the cost. This, of course, is a huge gain and enables both new problems to be studied, and existing problems to be examined either in more detail or at much lower cost.

Such subgrid models have had to make approximations — for example, bottom friction was computed using mean depth and velocity in Sehili et al. (2014), rather than as an integral over the detailed bathymetry. More advanced closures require additional assumptions. Defina (2000) and Volp et al. (2013, 2016) employed approximations including a steady friction gradient to obtain closed-form solutions for integral friction that are exact for special cases such as steady channel flow, and devised techniques to evaluate subgrid friction along individual strips of a cell. Wu et al. (2017, 2016) extended Volp's results to include the effects of vegetation drag in salt marshes, and applied the new system to a section of Delaware Bay. D'Alpaos and Defina (2007) further examined the effect of unresolved momentum mixing and found that these contributions could in some cases be modeled by increasing the effective bottom friction for coarse grid solutions. These previous studies have shown considerable improvements in the resolution-accuracy tradeoff, but there remain significant uncertainties in closures and even in the basic forms of the equations to be used.

The present paper develops shallow water subgrid systems for storm surge using formal averaging methods (e.g. Whitaker, 1999). These methods produce equations that are similar in many ways to those found in previous studies, but have additional terms and closures that had been previously neglected, and arise from the averaging process. Different levels of closures are identified, as well as the information required for their implementation. The systems are tested for accuracy and intercompared at different resolutions. In the remainder of this paper, Section 2 derives the subgrid theory and discusses the different levels of closure. Section 3 tests the systems on idealized geometries, and over the more complex real-world environment of Buttermilk Bay, Massachusetts, USA. Finally, Section 4 summarizes the present work and gives a framework for future research, development, and implementation activities.



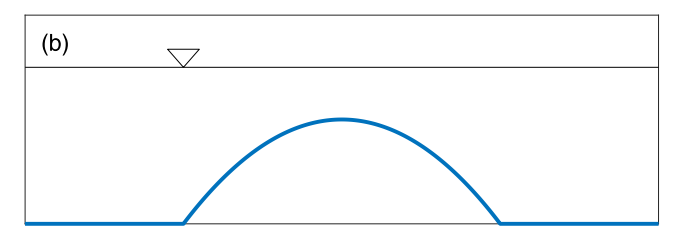


**Fig. 1.** Cross-sectional bed elevation and water levels of a larger grid where (a) At least two independent surface elevations and velocities are required to represent processes; (b) It may be possible to represent subgrid quantities using a single bulk surface elevation and velocity.

#### 2. Theory

High resolution storm surge systems are generally governed by the depth integrated shallow water equations, to be solved here in conservative form. The conservation of mass equation is

$$\frac{\partial H}{\partial t} + \frac{\partial HU}{\partial x} + \frac{\partial HV}{\partial y} = 0 \tag{1}$$

where  $\mathbf{U} \equiv (U,V)$  is the depth-averaged horizontal velocity vector, and the local total water depth is  $H \equiv h + \eta$  where h is the still water depth and  $\eta$  is the free surface elevation. The conservative form of the momentum equation is

$$\begin{split} &\frac{\partial HU}{\partial t} + \frac{\partial}{\partial x} \left( HUU \right) + \frac{\partial}{\partial y} \left( HUV \right) + gH \frac{\partial \eta}{\partial x} \\ &= -\frac{\tau_{bx} - \tau_{sx}}{\rho} - \frac{1}{\rho} \frac{\partial P_A}{\partial x} + f_c HV + \frac{1}{\rho} \left( \frac{\partial H\tau_{xx}}{\partial x} + \frac{\partial H\tau_{xy}}{\partial y} \right), \\ &\frac{\partial HV}{\partial t} + \frac{\partial}{\partial x} \left( HVU \right) + \frac{\partial}{\partial y} \left( HVV \right) + gH \frac{\partial \eta}{\partial y} \end{split} \tag{2}$$

$$= -\frac{\tau_{by} - \tau_{sy}}{\rho} - \frac{1}{\rho} \frac{\partial P_A}{\partial y} - f_c H U + \frac{1}{\rho} \left( \frac{\partial H \tau_{xy}}{\partial x} + \frac{\partial H \tau_{yy}}{\partial y} \right)$$
(3)

where  $\tau_b = (\tau_{bx}, \tau_{by})$  is the bed stress,  $\tau_s = (\tau_{sx}, \tau_{sy})$  is the surface stress,  $\tau_{xx}$ ,  $\tau_{xy}$ , and  $\tau_{yy}$  are depth-averaged Reynolds stresses,  $P_A$  is local atmospheric pressure, and  $f_c$  is the Coriolis parameter. When the topography and bathymetry are represented faithfully at high enough resolution, and given the appropriate atmospheric forcing and bottom friction, numerical systems based on these equations have been shown to provide accurate representations of storm surge for a variety of situations (see for example Bunya et al., 2010; Dietrich et al., 2010; Hope et al., 2013).

# 2.1. Averaging tools

Subgrid equations are derived from the original high resolution equations (1)–(3) following techniques laid out in Whitaker (1999) that were originally developed for use in the generation of equations for flow in porous media. These result in new sets of equations for coarsened quantities, but with corrections over the subgrid scale. The averaging scale to be used here is  $A_G$ , the so-called grid averaging area. Numerically, this averaging scale must be at least as large as the coarse grid size, but may be larger. Computational (coarsened) variables will

be defined on this grid-averaged scale, with smaller scale variations smoothed out.

For some dummy quantity, Q, hydrodynamic variables coarsened to the grid scale are defined as

$$\langle Q \rangle_G \equiv \frac{1}{A_G} \iint_{A_{W}} Q dA \tag{4}$$

where  $A_W$  is the wet portion of  $A_G$ . This will be called the "grid average" and is denoted with subscript "G". An alternate average used here is the "wet average" which uses the wet portion of the averaging area, and is defined as

$$\langle Q \rangle_W \equiv \frac{1}{A_W} \iint_{A_W} Q dA \tag{5}$$

This average will be denoted with subscript "W". The terms "grid average" and "wet average" are respectively equivalent to the "phase average" and "intrinsic phase average" found in, e.g., Whitaker (1999). For fully inundated (completely wet) grids, these quantities will be identical.

The volume averaged velocity used here is defined as

$$\langle U \rangle \equiv \frac{\iint_{A_G} H U dA}{\iint_{A_G} H dA}$$
 (6)

Because the depth is by definition zero in dry areas, this quantity is identical if the integration limits are taken as the wet area rather than the entire grid. Although other definitions of velocity are possible, use of a volume averaged velocity eliminates the necessity for closures in some terms.

Often, it is helpful to define coarsened variables in terms of the wet averages, where integrals are defined only over the wet area. For example, the grid average of water surface elevation in partially-wet regions has much less physical meaning than the wet average. If we define the wet averaging area as

$$A_W = \phi A_G \tag{7}$$

where  $\phi$  is the wet fraction in the averaging area (which may vary strongly with local surface elevations), then for hydrodynamic quantity Q.

$$\langle Q \rangle_G = \phi \langle Q \rangle_W \tag{8}$$

The grid-averaged wet volume per unit area is now

$$V_W(\langle \eta \rangle) \equiv \int_{-\infty}^{\langle \eta \rangle} \varphi(z) dz = \langle H \rangle_G \,, \ \varphi(z) = \frac{1}{A_G} \int_{A_G} p(h(\mathbf{x}) + z) dA, \tag{9}$$

where  $\varphi$  is a wet fraction for a given value z and p(s)=1 for s>0 and 0 for  $s\leq 0$ . If subgrid bathymetry and topography are known and we assume that  $std\ \langle \eta\rangle \ll \langle H\rangle_W$ , then  $\phi\equiv \varphi(\langle \eta\rangle)$  can be defined and used to develop a lookup table. These are single valued relations and so can be flipped as desired,

$$\langle \eta \rangle = f(V_W) \tag{10}$$

where it is understood that the average for  $\langle \eta \rangle$  is taken over the wet fraction, not the full averaging area. This can also be implemented as a lookup table and may be useful numerically.

The development of subgrid equations involves taking grid averages of the mass and momentum equations (1)–(3), and determining closures for terms that are not uniquely defined by the coarsened variables, with details of the averaging techniques given in Whitaker (1999). Two rules are used repeatedly for translating hydrodynamic quantities between fine and coarse scales:

$$\langle \nabla Q \rangle_G = \nabla \langle Q \rangle_G + \frac{1}{A_G} \oint_{\Gamma_W} \mathbf{n} Q ds \tag{11}$$

$$\left\langle \frac{\partial Q}{\partial t} \right\rangle_{G} = \frac{\partial \left\langle Q \right\rangle_{G}}{\partial t} - \frac{1}{A_{G}} \oint_{\Gamma_{W}} Q \mathbf{U}_{B} \cdot \mathbf{n} ds \tag{12}$$

where  $\Gamma_W$  is the wet–dry boundary,  ${\bf n}$  is the boundary normal, and  ${\bf U}_B$  is the velocity of the potentially moving boundary. These rules relate averages of operators acting on fine scale quantities to those acting on coarse quantities, and introduce additional terms at the wet–dry boundary. We note that, by averaging the conservative form of the momentum equation rather than the nonconservative form, all boundary integral terms that are proportional to the local water depth, H, are zero by definition and do not require additional closures for these terms.

## 2.2. Averaged mass equation

The averaged mass equation can be written in various interchangeable forms. Using the definition of volume-averaged velocity, relationships between wet and grid averages, and the coarsening rules (6)–(12), while averaging to the grid level but using wet-averaged hydrodynamic variables, the system becomes

$$\frac{\partial \phi \langle H \rangle_{W}}{\partial t} + \frac{\partial \phi \langle H \rangle_{W} \langle U \rangle}{\partial x} + \frac{\partial \phi \langle H \rangle_{W} \langle V \rangle}{\partial y} = 0. \tag{13}$$

Again, boundary integrals in (11)–(12) become zero and do not appear in (13) because H is zero at the wet–dry boundary.

Using the definition of grid averaged quantities (8), the mass equation may be written in terms of the grid-averaged depth as

$$\frac{\partial \langle H \rangle_G}{\partial t} + \frac{\partial \langle U \rangle \langle H \rangle_G}{\partial x} + \frac{\partial \langle V \rangle \langle H \rangle_G}{\partial y} = 0 \tag{14}$$

or equivalently as

$$\frac{\partial V_W}{\partial t} + \frac{\partial \langle U \rangle \langle H \rangle_G}{\partial x} + \frac{\partial \langle V \rangle \langle H \rangle_G}{\partial y} = 0.$$
 (15)

From (9) and using Leibniz's rule, the mass equation can be also written with a time derivative of  $\langle \eta \rangle$  as follows

$$\phi \frac{\partial \langle \eta \rangle}{\partial t} + \frac{\partial \phi \langle H \rangle_W \langle U \rangle}{\partial x} + \frac{\partial \phi \langle H \rangle_W \langle V \rangle}{\partial y} = 0.$$
 (16)

which is equivalent to the form presented by Defina (2000), who used flux as a variable rather than velocity as here.

All of the forms of the mass equation are quite straightforward: if we can uniquely define water volume per unit area (grid-averaged depth) as a function of surface elevation as in (10), then the conservation of mass system is closed and requires no additional manipulation.

## 2.3. Momentum equations

The averaged momentum equations are derived from (3) using the volume-averaged velocity (6), the definitions for averaged quantities and wet averages, the coarsening rules (6)–(12), and the averaged mass equation (16). Because the conservative form of the momentum equation has zero depth at the shoreline, boundary terms in (11)–(12) vanish, simplifying the coarsened equations greatly. Coarsened equations are given in quasi-conservative form by

$$\begin{split} &\frac{\partial \phi \langle U \rangle \langle H \rangle_{W}}{\partial t} + \frac{\partial}{\partial x} \left( \phi \langle UUH \rangle_{W} \right) + \frac{\partial}{\partial y} (\phi \langle UVH \rangle_{W}) = \\ &- g\phi \left\langle H \frac{\partial \eta}{\partial x} \right\rangle_{W} - \phi \left\langle \frac{\tau_{bx} - \tau_{sx}}{\rho} \right\rangle_{W} - \phi \frac{\langle H \rangle_{W}}{\rho} \frac{\partial P_{A}}{\partial x} - \phi f_{c} \langle V \rangle \langle H \rangle_{W} \\ &+ \frac{1}{\rho} \left( \frac{\partial}{\partial x} \left( \phi \langle H \tau_{xx} \rangle_{W} \right) + \frac{\partial}{\partial y} \left( \phi \langle H \tau_{xy} \rangle_{W} \right) \right) \end{split} \tag{17}$$

$$\begin{split} &\frac{\partial \phi \langle V \rangle \langle H \rangle_{W}}{\partial t} + \frac{\partial}{\partial x} (\phi \langle UVH \rangle_{W}) + \frac{\partial}{\partial y} (\phi \langle VVH \rangle_{W}) = \\ &- g\phi \left\langle H \frac{\partial \eta}{\partial y} \right\rangle_{W} - \phi \left\langle \frac{\tau_{by} - \tau_{sy}}{\rho} \right\rangle_{W} - \phi \frac{\langle H \rangle_{W}}{\rho} \frac{\partial P_{A}}{\partial y} + \phi f_{c} \langle U \rangle \langle H \rangle_{W} \\ &+ \frac{1}{\rho} \left( \frac{\partial}{\partial x} \left( \phi \langle H \tau_{xy} \rangle_{W} \right) + \frac{\partial}{\partial y} \left( \phi \langle H \tau_{yy} \rangle_{W} \right) \right). \end{split} \tag{18}$$

We note that, if it is assumed that the Coriolis parameter,  $f_c$ , varies on larger spatial scales than velocities and depths, the Coriolis term needs

no additional closure arising from the definition of volume-averaged velocity. Making the same assumption for the atmospheric pressure term leads to terms that similarly do not require additional closures. However, convective momentum, bottom friction, surface gradients, and Reynolds stresses all require further assumptions to close the system.

A quasi-nonconservative form of the momentum equation, generated by averaging the conservative form of the momentum equation and then dividing through by the mean depth, is given in Appendix A. This resembles the nonconservative form of the shallow water momentum equation with additional closure terms arising from the averaging process, and may be useful for certain numerical schemes. We note that this is different than if we had simply averaged the nonconservative form of the momentum equation, which results in difficult boundary terms and is not shown here.

#### 2.4. Closures

We make closure approximations so that all quantities are written in terms of the coarsened variables. The closure approximations are required because subgrid fluctuations in bathymetry and/or land cover induce fluctuations in velocity, friction, and depth, whose values are highly correlated and non-negligible. Many of these terms cannot be evaluated exactly and must be closed. To a large degree, the accuracy of the subgrid system will depend on both the general form assumed for the closures, and the specific choices made to close the system. The general forms for closures are chosen to resemble standard systems as much as possible in order to enable modification of existing codes, while retaining the generality to pursue advanced closure options.

For the convective momentum terms, the closure assumption is made to look like the standard system with additional correction coefficients

$$\begin{pmatrix}
\langle UUH \rangle_{W} & \langle UVH \rangle_{W} \\
\langle VUH \rangle_{W} & \langle VVH \rangle_{W}
\end{pmatrix}$$

$$= \begin{pmatrix}
C_{UU} \langle U \rangle \langle U \rangle \langle H \rangle_{W} & C_{UV} \langle U \rangle \langle V \rangle \langle H \rangle_{W} \\
C_{VU} \langle V \rangle \langle U \rangle \langle H \rangle_{W} & C_{VV} \langle V \rangle \langle V \rangle \langle H \rangle_{W}
\end{pmatrix}$$
(19)

The general form of this closure is equivalent to that of Defina (2000), who instead derived the system in flux variables.

Surface gradient terms are approximated as:

$$\left\langle H \frac{\partial \eta}{\partial x} \right\rangle_{W} = \left\langle H \right\rangle_{W} \left( C_{\eta, xx} \frac{\partial \left\langle \eta \right\rangle}{\partial x} + C_{\eta, xy} \frac{\partial \left\langle \eta \right\rangle}{\partial y} \right) \tag{20}$$

$$\left\langle H \frac{\partial \eta}{\partial y} \right\rangle_{W} = \left\langle H \right\rangle_{W} \left( C_{\eta, yx} \frac{\partial \left\langle \eta \right\rangle}{\partial x} + C_{\eta, yy} \frac{\partial \left\langle \eta \right\rangle}{\partial y} \right) \tag{21}$$

This closure term may be the most surprising, but, as will be shown, it is clearly needed in some cases because the area averages of gradients on a grid average may be dominated by a few small subregions. Cross terms will not be needed in many cases, but may be required in regions where bottom friction, and thus surface gradients, are anisotropic because of subgrid features.

The bottom stress closure is given as a quadratic bottom friction law, generalized to

$$\left\langle \frac{\tau_{bx}}{\rho} \right\rangle_{W} = \left\langle \frac{\rho c_{f} |U| U}{\rho} \right\rangle_{W} = \left| \left\langle U \right\rangle \right| \left( c_{M,f,xx} \left\langle U \right\rangle + c_{M,f,xy} \left\langle V \right\rangle \right) \tag{22}$$

$$\left\langle \frac{\tau_{by}}{\rho} \right\rangle_{W} = \left\langle \frac{\rho c_f |U|V}{\rho} \right\rangle_{W} = |\langle U \rangle| \left( c_{M,f,yx} \langle U \rangle + c_{M,f,yy} \langle V \rangle \right) \tag{23}$$

where  $c_{M,f,xx}(\langle \eta \rangle)$ , etc., are to-be-determined equivalent frictional coefficients that may be strong functions of water surface elevation. Other quadratic frictional closures, e.g., Manning, may be translated into this form. Once again, cross terms are possible because of anisotropy.

Coarse-scale Reynolds stress terms are approximated as

$$\begin{pmatrix}
\langle H \tau_{xx} \rangle_{W} & \langle H \tau_{xy} \rangle_{W} \\
\langle H \tau_{xy} \rangle_{W} & \langle H \tau_{yy} \rangle_{W}
\end{pmatrix}$$

$$= \langle H \rangle_{W} \mu_{t} \begin{pmatrix}
\frac{2\partial \langle U \rangle}{\partial x} & \left(\frac{\partial \langle U \rangle}{\partial y} + \frac{\partial \langle V \rangle}{\partial x}\right) \\
\left(\frac{\partial \langle V \rangle}{\partial x} + \frac{\partial \langle U \rangle}{\partial y}\right) & \frac{2\partial \langle V \rangle}{\partial y}
\end{pmatrix}$$
(24)

where  $\mu_t(x, y, t)$  is a grid scale eddy viscosity. Other Reynolds stress approximations that do not use eddy viscosity are also possible, but are not explored here.

After substituting the closure terms into momentum equations (17)–(18) and canceling some terms using the averaged mass equation, the momentum equations become

$$\begin{split} \phi \left\langle H \right\rangle_{W} & \frac{\partial \left\langle U \right\rangle}{\partial t} - \left\langle U \right\rangle \nabla \cdot \left( \phi \left\langle U \right\rangle \left\langle H \right\rangle_{W} \right) \\ & + \frac{\partial}{\partial x} (C_{UU} \phi \left\langle U \right\rangle \left\langle U \right\rangle \left\langle H \right\rangle_{W}) + \frac{\partial}{\partial y} (C_{UV} \phi \left\langle U \right\rangle \left\langle V \right\rangle \left\langle H \right\rangle_{W}) \\ & = -g \phi \left\langle H \right\rangle_{W} \left( C_{\eta, xx} \frac{\partial \left\langle \eta \right\rangle}{\partial x} + C_{\eta, xy} \frac{\partial \left\langle \eta \right\rangle}{\partial y} \right) \\ & - \phi |\left\langle U \right\rangle |\left( c_{M, f, xx} \left\langle U \right\rangle + c_{M, f, xy} \left\langle V \right\rangle \right) \\ & - \phi \frac{\left\langle H \right\rangle_{W}}{\rho} \frac{\partial P_{A}}{\partial x} - \phi f_{c} \left\langle V \right\rangle \left\langle H \right\rangle_{W} + \frac{\phi \tau_{sx}}{\rho} \\ & + \frac{1}{\rho} \frac{\partial}{\partial x} \left( \phi \left\langle H \right\rangle_{W} \mu_{t} \frac{2\partial \left\langle U \right\rangle}{\partial x} \right) \\ & + \frac{1}{\rho} \frac{\partial}{\partial y} \left( \phi \left\langle H \right\rangle_{W} \mu_{t} \left( \frac{\partial \left\langle U \right\rangle}{\partial y} + \frac{\partial \left\langle V \right\rangle}{\partial x} \right) \right) \end{split} \tag{25}$$

$$\begin{split} \phi \left\langle H \right\rangle_{W} & \frac{\partial \left\langle V \right\rangle}{\partial t} - \left\langle V \right\rangle \nabla \cdot \left( \phi \left\langle U \right\rangle \left\langle H \right\rangle_{W} \right) \\ & + \frac{\partial}{\partial x} \left( C_{VU} \phi \left\langle U \right\rangle \left\langle V \right\rangle \left\langle H \right\rangle_{W} \right) + \frac{\partial}{\partial y} \left( C_{VV} \phi \left\langle V \right\rangle \left\langle V \right\rangle \left\langle H \right\rangle_{W} \right) \\ & = -g \phi \left\langle H \right\rangle_{W} \left( C_{\eta, yx} \frac{\partial \left\langle \eta \right\rangle}{\partial x} + C_{\eta, yy} \frac{\partial \left\langle \eta \right\rangle}{\partial y} \right) \\ & - \phi |\left\langle U \right\rangle |\left( c_{M, f, yx} \left\langle U \right\rangle + c_{M, f, yy} \left\langle V \right\rangle \right) \\ & - \phi \frac{\left\langle H \right\rangle_{W}}{\rho} \frac{\partial P_{A}}{\partial y} + \phi f_{c} \left\langle U \right\rangle \left\langle H \right\rangle_{W} + \frac{\phi \tau_{sy}}{\rho} \\ & + \frac{1}{\rho} \frac{\partial}{\partial x} \left( \phi \left\langle H \right\rangle_{W} \mu_{t} \left( \frac{\partial \left\langle U \right\rangle}{\partial y} + \frac{\partial \left\langle V \right\rangle}{\partial x} \right) \right) \\ & + \frac{1}{\rho} \frac{\partial}{\partial y} \left( \phi \left\langle H \right\rangle_{W} \mu_{t} \frac{2\partial \left\langle V \right\rangle}{\partial y} \right) \end{split} \tag{26}$$

In summary, the set of governing equations based on averaging of the SWE with wet-averaged variables consists of (13), (25), and (26).

In the discretization of the governing equations with a staggered finite difference (FD) scheme, as described in Appendix B, it is more convenient to work with their equivalent form in which the grid-averaged total depth  $\langle H \rangle_G$  is used. By using the fact that  $\langle H \rangle_G = \phi \langle H \rangle_W$ , the momentum equations (25)–(26) can be respectively rewritten as

$$\langle H \rangle_{G} \frac{\partial \langle U \rangle}{\partial t} - \langle U \rangle \nabla \cdot (\langle U \rangle \langle H \rangle_{G})$$

$$+ \frac{\partial}{\partial x} (C_{UU} \langle U \rangle \langle U \rangle \langle H \rangle_{G}) + \frac{\partial}{\partial y} (C_{UV} \langle U \rangle \langle V \rangle \langle H \rangle_{G})$$

$$= -g \langle H \rangle_{G} \left( C_{\eta, xx} \frac{\partial \langle \eta \rangle}{\partial x} + C_{\eta, xy} \frac{\partial \langle \eta \rangle}{\partial y} \right)$$

$$- \phi |\langle U \rangle | \left( c_{M, f, xx} \langle U \rangle + c_{M, f, xy} \langle V \rangle \right)$$

$$- \frac{\langle H \rangle_{G}}{\rho} \frac{\partial P_{A}}{\partial x} - \langle H \rangle_{G} f_{c} \langle V \rangle + \frac{\phi \tau_{sx}}{\rho}$$

$$+ \frac{1}{\rho} \frac{\partial}{\partial x} \left( \langle H \rangle_{G} \mu_{t} \frac{2\partial \langle U \rangle}{\partial x} \right) + \frac{1}{\rho} \frac{\partial}{\partial y} \left( \langle H \rangle_{G} \mu_{t} \left( \frac{\partial \langle U \rangle}{\partial y} + \frac{\partial \langle V \rangle}{\partial x} \right) \right)$$

$$\langle H \rangle_{G} \frac{\partial \langle V \rangle}{\partial x} - \langle V \rangle \nabla \cdot (\langle U \rangle \langle H \rangle_{G})$$

$$(27)$$

$$\begin{split} &+ \frac{\partial}{\partial x} (C_{VU} \langle U \rangle \langle V \rangle \langle H \rangle_G) + \frac{\partial}{\partial y} (C_{VV} \langle V \rangle \langle V \rangle \langle H \rangle_G) \\ &= -g \langle H \rangle_G \left( C_{\eta,yx} \frac{\partial \langle \eta \rangle}{\partial x} + C_{\eta,yy} \frac{\partial \langle \eta \rangle}{\partial y} \right) \\ &- \phi |\langle U \rangle | \left( c_{M,f,yx} \langle U \rangle + c_{M,f,yy} \langle V \rangle \right) \\ &- \frac{\langle H \rangle_G}{\rho} \frac{\partial P_A}{\partial y} + \langle H \rangle_G f_c \langle U \rangle + \frac{\phi \tau_{sy}}{\rho} \\ &+ \frac{1}{\rho} \frac{\partial}{\partial x} \left( \langle H \rangle_G \mu_t \left( \frac{\partial \langle U \rangle}{\partial y} + \frac{\partial \langle V \rangle}{\partial x} \right) \right) + \frac{1}{\rho} \frac{\partial}{\partial y} \left( \langle H \rangle_G \mu_t \frac{2\partial \langle V \rangle}{\partial y} \right) \end{split} \tag{28}$$

Thus, when using the grid-averaged total depth  $\langle H \rangle_G$ , the set of governing equations consists of (14), (27), and (28).

#### 2.4.1. Standard solution

The standard, non-subgrid, solutions may be recovered by using the closures

$$\begin{split} \bullet & \quad \phi = 0, \quad \langle \eta \rangle \leq - \langle h \rangle_G \\ \phi = 1, \quad \langle \eta \rangle > - \langle h \rangle_G \\ \bullet & \quad C_{\eta,xx} = C_{\eta,yy} = 1, \quad C_{\eta,xy} = C_{\eta,yx} = 0 \\ \bullet & \quad C_{M,f,xx} = C_{M,f,yy} = \left\langle C_f \right\rangle_G, \quad C_{M,f,xy} = C_{M,f,yx} = 0 \\ \bullet & \quad C_{UU} = C_{VV} = C_{UV} = C_{VU} = 1 \end{split}$$

where here the mean bed elevation,  $-\langle h \rangle_G$ , and the mean friction coefficients,  $C_{M,f,xx}$ , etc., are computed over the entire grid averaging area rather than the wet area. The turbulent eddy viscosity, or other approximation to Reynolds stresses, will use any scheme desired by the user. These equations exactly revert to standard shallow water equations as implemented in a particular numerical scheme.

### 2.4.2. Level 0 closure

A basic subgrid closure is used for determining the wet fraction, but with very simple assumptions about flow. Essentially, it assumes that partial wetting and drying within a cell are determined by the wet fraction as calculated from subgrid data with an assumed near-flat water surface in the averaging area

• 
$$\phi(\langle \eta \rangle) = A_W(\langle \eta \rangle)/A_G$$

with all other closures the same as in the standard solution. This closure is similar to that used in Casulli (2009) and Sehili et al. (2014).

## 2.4.3. Level 1 closure

Level 1 closures use the fractional wetting and drying of Level 0, but also employ assumptions about the flow structure using canonical or near-canonical solutions. Defina (2000) and Volp et al. (2013) assumed a constant friction slope at all points on the subgrid, which may be thought of as flow in a quasi-1D channel, but with varying depths across the profile. This assumption defines the overall velocities at all locations in relation to the averaged velocity. Local velocities and depths are substituted back into the full equations, and comparison with the form of the closures yields closure coefficients. This particular closure can work well for flow that is almost parallel to depth contours, but is not expected to be as accurate for flow perpendicular to depth contours. The closure is different depending on which form of the averaged velocity variable is used. The Level 1 closure can be written as:

• 
$$\phi(\langle \eta \rangle) = A_W(\langle \eta \rangle)/A_G$$
  
•  $C_{\eta,xx} = C_{\eta,yy} = 1$ ,  $C_{\eta,xy} = C_{\eta,yx} = 0$   
•  $C_{M,f,xx} = C_{M,f,yy} = \langle H \rangle_G R_v^2$ ;  $C_{M,f,xy} = C_{M,f,yx} = 0$ , where
$$R_v = \frac{\langle H \rangle_W}{\left\langle H^{3/2} C_f^{-1/2} \right\rangle_W}$$
(29)

is dimensional with units  $L^{-1/2}$ .

• 
$$C_{UU} = C_{VV} = C_{VU} = C_{UV} = \frac{1}{\langle H \rangle_W} \left\langle \frac{H^2}{C_f} \right\rangle_W R_v^2$$
, Again, the turbulent eddy viscosity,  $\mu_t$ , is not uniquely defined by this closure.

#### 2.4.4. Level 2 closure

The Level 2 closure uses high resolution modeling to evaluate numerically all closure coefficients, which are then used in the coarse resolution subgrid system. To accomplish this, a high resolution model is run, potentially for a variety of water levels and hydrodynamic conditions, then the values of the closure terms are determined for a defined averaging area, which may be equal to the coarse grid and retained as a lookup table. For all closures, we assume  $C_* = f(x, y, \langle \eta \rangle)$ . If the forms of the closures are chosen well, and the closure terms have been accurately evaluated, then the subgrid system should very closely reproduce the high resolution model.

There are many possible ways that these closures could be computed, and the determination of closure coefficients remains an area of very active research. Although more sophisticated closures are to be introduced in future work, this introductory paper uses time- and water level-invariant closures with coefficients determined using a least squares regression. For example, the x-convective momentum closure chooses  $C_{UU}$  to minimize least-square error in  $\langle UUH \rangle_W = C_{UU} \langle U \rangle \langle U \rangle \langle H \rangle_W$  and so on. The entire time series of model outputs is used for the minimization, and different coefficients will be obtained at each coarse grid cell. Cross terms  $C_{\eta,xy}$ ,  $C_{\eta,yx}$ ,  $C_{M,f,xy}$ , and  $C_{M,yx}$  are set to zero: although there has been progress on computing anisotropic friction (e.g., Viero and Valipour, 2017) and anisotropic resistance due to obstacles (Viero, 2019) in specific cases, we do not yet have tools to evaluate anisotropy for general Level 2 closures.

This method of evaluating closure coefficients is not the only possible solution: coefficients that are water level-dependent will be necessary in regions where wetting and drying dominate. Simplified solutions of flow in subregions may also prove to be a viable methodology to determine closure coefficients: research into Level 2 closures is likely a decadal effort, and proper choice of closures may be a controlling factor for accuracy in many instances.

## 3. Tests and validation

This section presents several tests that challenge different aspects of the newly developed system. Tests include idealized scenarios that isolate specific portions of the system, and flooding cycles in a complex real-world bathymetry. All tests are driven by gravity — neither atmospheric pressure nor wind stress is applied in this introductory paper; however, these are not expected to change conclusions greatly as they are easily closed for use in the subgrid system. Wind-induced overland flooding may, however, introduce additional complex geometries and wetting/drying considerations for real-world cases. Tests here are divided into three sections:

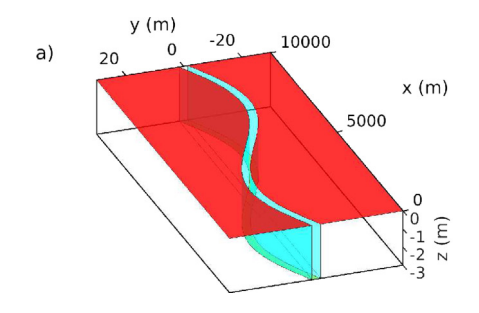
- 1. Flows in quasi-one-dimensional channels,
- 2. Flows through a two-dimensional bay-channel system,
- Flows through the complex geometry of Buttermilk Bay, Massachusetts, USA.

All tests compare standard shallow water solutions with Level 0 and higher level closures. The two-dimensional bay—channel test also makes a first attempt at a Level 2 closure. Ground truth for all simulations is taken to be the high resolution solution of the shallow water equations.

Note that all results presented below use Manning's formula

$$C_f = \frac{gn^2}{H^{1/3}},\tag{30}$$

where n denotes the Manning's roughness coefficient. Unless otherwise indicated, the Manning's roughness coefficient and magnitude of gravitational acceleration are set as  $n=0.02~{\rm m}^{-1/3}{\rm s}$  and  $g=9.81~{\rm m/s}^{-2}$ . For these introductory tests, which are focused in large part on testing filling and frictional closures, terms accounting for horizontal momentum diffusion are excluded.



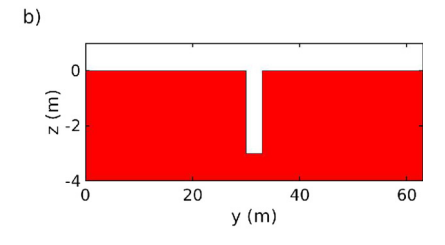


Fig. 2. Sinuous channel-floodplain geometry for steady flow tests. (a) Overall geometry; (b) Channel cross-section.

### 3.1. Idealized test: Flow in quasi-one-dimensional channels

In this test, the subgrid system is applied to solve three idealized quasi-one-dimensional open-channel flow problems: (i) steady flow through a compound channel, (ii) periodic flow through a channel with a parabolic cross-section and vertical sidewalls, and (iii) periodic flow through a compound channel with a parabolic cross-section and flat floodplain.

These three tests are used to examine the wetting and drying performance of the subgrid system in different channel configurations, and to demonstrate the importance of corrections even in these seemingly relatively simple idealized applications. All subgrid calculations in this section consider geometries where the cross section of the channel resides within one grid cell. These tests explore the feasibility of treating a simple channel flow entirely at the subgrid level within a framework of a two-dimensional numerical solver. Here, Levels 0 (partial filling of cell) and 1 (canonical channel flow closure) closures are considered in the calculations.

#### 3.1.1. Steady flow in a sinuous compound channel

This first test, which is adapted from Volp et al. (2013), considers a compound channel consisting of a sinusoidal channel and two floodplains. The channel geometry and cross section are depicted in Fig. 2.

The meandering narrow channel has a rectangular cross section of 63 m width and its bed level is 3 m below the adjacent floodplains. The slope of the compound channel is 0.0001 downhill in the x-direction; thus, there is a 1 m change in bed elevation over the channel length. Constant surface elevations  $\eta_c$  and  $\eta_c-1$  m are imposed at the channel inlet and outlet, respectively, which generate steady flow with a surface elevation parallel to the bed slope. Because flow is quasi-1D, the advection term is very small, and the solution is largely a balance between the surface gradient and bottom friction. Here, the numerical experiment focuses only on the case where the floodplains are fully flooded, i.e.  $\eta_c$  is greater than the elevation of the floodplains at the inlet. In this case, correcting the friction term to account for variations in the water depth will improve representation of volumetric discharge values.

The numerical solution computed on the fine grid of  $\Delta x = \Delta y = 1$  m resolution is used as a reference solution, while the coarse grid used only one 63 m  $\times$  10000 m cell that covered the entire fine grid domain. Because surface elevations were imposed at the boundaries and there is only one grid cell, elevations are not an appropriate point of comparison between standard and subgrid solutions; however, this is not the case for the discharge, which depends strongly on the bottom stress and its distribution in space. Fig. 3 shows the relative discharge error

$$R = \frac{(Q_N - Q_{\text{ref}})}{Q_N} \times 100\%,$$

where  $Q_N$  is the volumetric discharge across the channel cross section ( $\int uHdy$ ) for the subgrid and standard solutions and  $Q_{\rm ref}$  is the discharge of the reference solution. In Fig. 3, the magenta diamonds

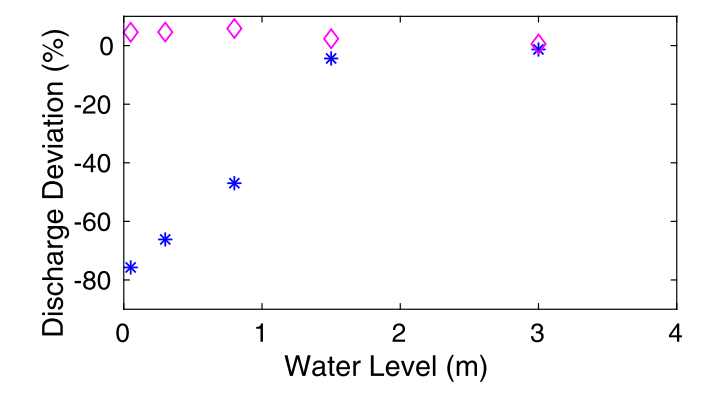


**Fig. 3.** The relative deviation of the discharge in the subgrid solution compared to the reference solution for steady flow in a sinuous channel. Level 0 (blue star), and Level 1 (magenta diamond).

depict the results from closure Level 1 and the blue stars depict closure Level 0. It is noted that in this test case, because every computational cell is completely wet, the subgrid technique with Level 0 closure and standard method become identical due to the fact that the area fraction  $\phi$  is unity and  $\langle H \rangle_W$  is simply  $\eta + \langle h \rangle_G$ . It can be seen that the Level 0 closure underpredicts the discharge, especially at low water levels. Because the advection term is negligible and surface elevations of the reference solution and coarse grid solution are identical, it can be concluded that bottom friction is the only term that is not a good approximation in the coarse grid solution. Because the difference in water depth between channel and flat floodplains is relatively large for these low water levels, the Level 0 closure overestimates the bottom friction and as a consequence underestimates velocity and discharge. As the water level increases, the relative difference in depth decreases, and the predicted closure Level 0 discharge value becomes closer to that of the reference solution. It can be observed that the discharge obtained from Level 1 is close to that of the reference solution for all water levels, which is as expected since this closure was derived under the assumption of uniform channel flow.

#### 3.1.2. Parabolic channel

In this example, quasi-tidal flow in a long parabolic channel is considered, with a channel cross section as shown in Fig. 4. The channel length is 5376 m and width is 128 m. The channel inlet surface elevation is forced with a tide-like time series  $\eta(t) = \sin(2\pi t/T)$  (m), where T is a varying forcing period to assess sensitivity of the closures. A wall boundary condition is imposed on the far end of the channel. For this case, the reference solution uses a grid with  $2 \text{ m} \times 2 \text{ m}$  resolution, while the coarse simulations use a much coarser  $128 \text{ m} \times 128 \text{ m}$  grid; the full channel width is included in one coarse grid cell, but there are 42 coarse cells in the direction of flow. The underlying bathymetric data employed in the subgrid calculations is identical to that of the reference solution.

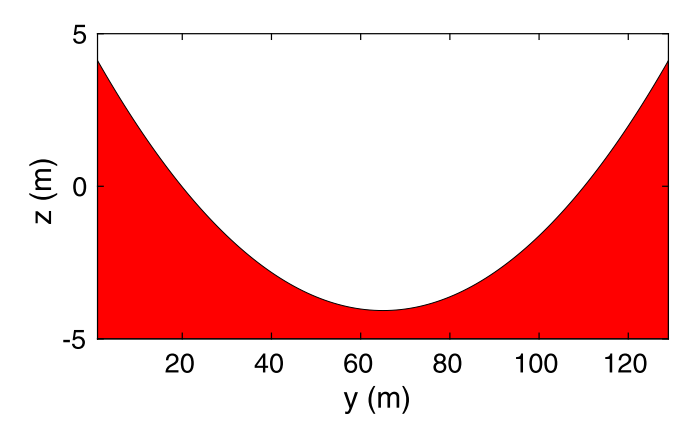
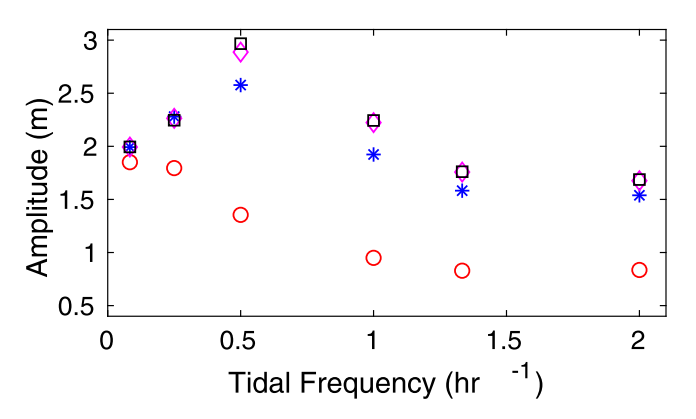


Fig. 4. Channel cross-section.



**Fig. 5.** Water surface amplitudes at the far end of the parabolic channel as the forcing frequency varies. Level 0 (blue star), Level 1 (magenta diamond), standard solution (red circle), high resolution (black square).

Fig. 5 shows water surface amplitudes (maximum minus minimum surface elevation) for the subgrid and standard solutions after flow reaches a periodic steady state at the far end of the channel. In this test example, portions of the channel are subjected to rising and receding water. The subgrid systems, which account for the mass correction through the partial filling of cells that are not fully submerged, can improve upon the standard solution. Indeed, as can be observed in Fig. 5, the amplitudes obtained from the subgrid system are in significantly better agreement with the reference solution in comparison to the standard solution. Level 0 closure (blue stars), which includes only the partial filling, accurately predicts amplitude especially at low forcing frequencies where the effect of nonlinearity in the system is low. However, the mass correction alone is insufficient as indicated by somewhat larger errors in Level 0 closure results for higher frequencies. These problems stem from inaccurate bottom friction and advection terms; in this test case, there is an overestimation of friction and an underestimation of advective stresses.

In contrast, the subgrid system with Level 1 closure, which is based on a constant frictional slope assumption, yields water surface amplitudes that match closely to the reference solution. This provides numerical evidence that, when the proper subgrid correction parameters are used, the system proposed here is able to produce an accurate solution on the coarse grid.

## 3.1.3. Compound parabolic channel

In this final quasi-1D example, a compound parabolic channel is considered for quasi-tidal flow as illustrated in Fig. 6. The channel has a length of 5376 m and an overall width of 256 m, and a flat floodplain exists at elevation z=0.25 m. As with the previous example, the open boundary is forced by the elevation boundary condition

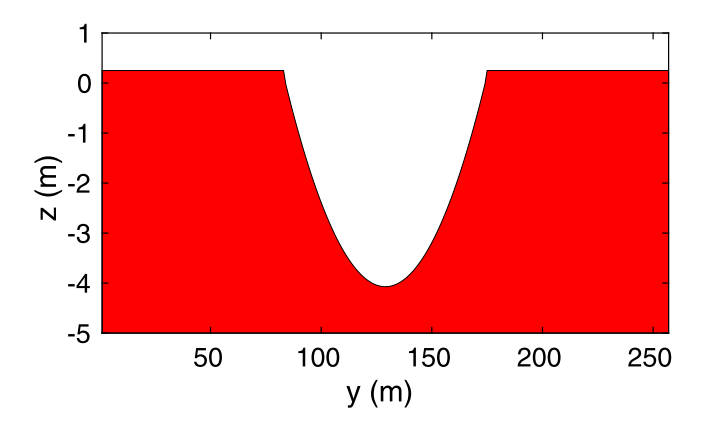
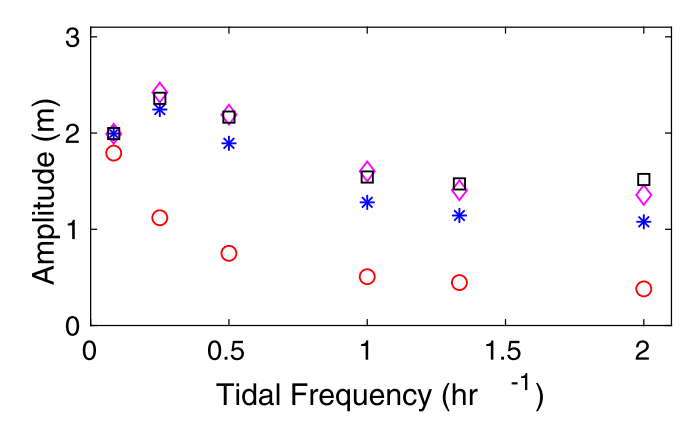


Fig. 6. Channel cross-section of compound parabolic channel.



**Fig. 7.** Water surface amplitudes at the far end of compound parabolic channel with varying forcing frequency. Level 0 (blue star), Level 1 (magenta diamond), standard solution (red circle), high resolution (black square).

 $\eta(t) = \sin{(2\pi t/T)}$  m with a wall boundary at the far end; thus water periodically generates overflow from the main channel to the flood plain. The grid size used in the coarse grid calculations and reference solution is 256m  $\times$  256m, and 2m  $\times$  2m, respectively.

Fig. 7 shows the computed coarse grid water surface amplitudes for subgrid Levels 0 and 1 closures at the closed end of the channel in comparison to the coarse grid standard solutions, and the high resolution reference solution. Overall, the results exhibit a pattern similar to the previous example: the standard solution yields rather poor amplitudes at all but the lowest forcing frequencies, while both Level 0 and especially Level 1 closures produce solutions that are in much better agreement with the reference solution. Solutions for Level 0 closure do show errors increasing with increasing forcing frequency.

Level 0 closure errors for this test are noticeably larger than those found for the Level 0 closure solution of the parabolic problem as shown in Fig. 8. This error increase comes from the very large relative variation in water depth between channel and wet floodplain and consequent variations in friction and convective stresses. Level 0 closures do not account for the large depth variations in computation of bottom stresses and convective momentum, and so have much greater error for this case. In contrast, the Level 1 closure can provide a much more accurate water surface amplitude as seen in Fig. 7 as it accounts for the effect of friction and convective stresses, and the channel-floodplain test closely resembles the assumptions used to derive the Level 1 closure itself.

## 3.2. Flow through repeating bay-channel systems

A first test of the Level 2 closure methodology is performed in an idealized system of bays and channels, which differs strongly from the

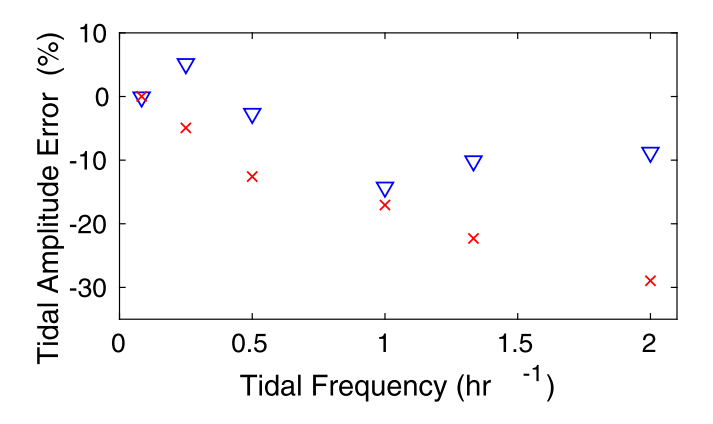


Fig. 8. Percentage error in amplitudes of Level 0 closure solution: parabolic channel (blue triangle), compound parabolic channel (red cross).

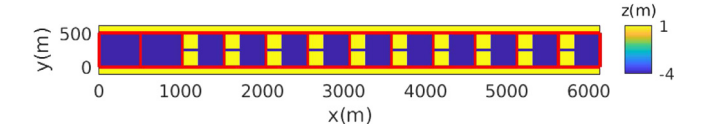


Fig. 9. Bed elevations for a system of repeating bays and channels. The red lines show coarse grid cell outlines, where a coarse cell consists of a full bay-channel pair.

quasi-1D systems tested previously. In this system, channels enable exchange of mass and momentum between subsequent bays. The channel-bay interface features an abrupt narrowing/expansion, meaning the characteristic velocity fields of the bays and channels vary greatly. The chain-like geometry of bays and channels, induces non-linear momentum effects that create challenges in predicting the surface elevations and velocities in each bay. Simulations of this system are run on a high resolution grid, where all geometrical descriptions are resolved. Additionally, simulations are computed on a coarse grid, where each coarse grid cell spans a single bay—channel pair. With such coarse resolution, the momentum equations require significant corrections when the interplay of the channel and bay-scale physics is significant.

## 3.2.1. Repeating bay-channel system setup

The bathymetry for the system of repeating bays and channels is shown in Fig. 9. In total, there are 10 bay–channel pairs, with each bay connected to the subsequent bay by a narrow channel. Wet portions of the domain (blue) have a bed elevation of z=-4 m. The elevation of the neighboring floodplains (yellow) is z=1 m, sufficiently high that it remains dry throughout the simulation. Each bay has length 320 m and width 480 m, where width is in the y direction and perpendicular to the primary flow direction. Each channel has length 192 m and width 32 m.

The seaward boundary borders a longer reservoir with length 1024 m and width 512 m which has a periodic elevation boundary condition imposed at x=0, driving primary flow. Sinusoidal quasitidal forcing cycles have a varying period T with a fixed range of 0.4 m, which is 10% of the still water depth. The accuracy and robustness of our initial Level 2 closure is examined by running simulations for varying forcing frequencies and comparing to high resolution simulations and other closure levels.

#### 3.2.2. Level 2 corrections

Level 2 corrections are employed on a coarse grid with dimensions  $512~\mathrm{m} \times 512~\mathrm{m}$ : this resolution fits one channel–bay pair exactly into one coarse cell. In this study, as a first attempt at Level 2 closure, correction coefficient values are time-independent. Level 2 coefficient values are selected for each grid cell from high resolution results using the methods described previously in Section 2.4.4, and we note that each coarse grid cell has a separate set of time-independent correction coefficients.

#### 3.2.3. Repeating bay-channel reference case

The reference test case for the bay–channel geometry has period T=3 h; it is selected because the high resolution and standard coarse grid solutions have significant differences in both the surface elevation amplitudes and timing. The high resolution simulation used for comparison and to train the Level 2 closure has  $8 \text{ m} \times 8 \text{ m}$  resolution.

Fig. 10(a) shows the water surface amplitude in each bay for the high resolution (black), standard (red), Level 0 closure (blue) and Level 2 closure (green) simulations (note that for this particular case, Levels 0 and 1 closures are identical because the wet area of each cell has uniform depth.) In general, the standard and Level 0 methods overestimate the amplitude in each bay. The Level 2 closure more accurately predicts amplitudes in bays closest to the reservoir, however water level fluctuations are overestimated in the back bays. The predicted amplitude by the standard method is always largest.

Fig. 10(b) displays the error in timing of high tide as a fraction of forcing period  $[t(\operatorname{peak})_N - t(\operatorname{peak})_{ref}]/T$ , where  $t(\operatorname{peak})$  corresponds to the time of the fourth high tide event for the high resolution and coarse simulations and T is the forcing period. The standard and Level 0 closure methods predict early arrival of high tide and this error increases as distance from the reservoir increases; however, including the Level 2 coefficients significantly reduces the error in arrival of high water. Specifically, the representative correction coefficients used in Level 2 closure effectively increase friction while also reducing the sea surface gradient effect, both of which delay the propagation of the wave.

As the distance from the reservoir increases, the standard and Level 0 closure methods generally display greater error in predicting the timing of high and low tide events, as well as the amplitude. Fig. 10(c–d) displays the time series of surface elevation for the fine and coarse resolution simulations in the bay farthest from the reservoir and in the reservoir, respectively. In the reservoir, all coarse simulations show excellent agreement with the high resolution run, as expected because this is where forcing is applied. In the back bay, the flow has been significantly affected by the channels and so the correction terms in the momentum equations become important. The standard and Level 0 closure simulations yield surface elevations that significantly deviate from the high resolution benchmark. The Level 2 closure method sufficiently corrects the timing of the flow; however, the amplitude is still overestimated.

In the repeating bay-channel system, the channels play an important role in transporting momentum through the domain. The narrowing at the bay-channel interface induces an area of high flow velocity and thus high deviations from the mean coarse cell velocity  $\langle U \rangle$ . These fluctuations manifest as large values of corrections to the friction and convective terms. Additionally, the channels experience large sea surface gradients but only comprise a small portion of the overall grid. Hence, the channel-scale physics must be incorporated into the momentum equation of the coarse simulations for accurate portrayal of sea surface evolution. The importance of averaged sea surface gradient may be seen in Fig. 10(a-b) for the magenta triangles, which represent sub-Level 2 computations (Level 2 with surface gradient coefficients set to  $C_{\eta,xx}=C_{\eta,yy}=1,~C_{\eta,xy}=C_{\eta,yx}=0$ ). These sub-Level 2 results are much worse than full Level 2, and are very close to those from Levels 1 and 0 simulations, demonstrating that even if convection and friction are considered, the new surface gradient average terms introduced here are needed in some situations to ensure that accurate solutions are obtained.

Given that primary flow is in the x direction, the important closure coefficients are  $C_{UU}$ ,  $C_{\eta,x}$  and  $n_{mx}$ . Fig. 11 shows the representative values of these correction coefficients divided by the coefficients of the standard solution ( $C_{UU}$ ,  $C_{\eta,x}=1$ , n=.02). The effective bottom friction roughness  $n_{m,x}$  is larger than the local roughness coefficient; the average effective roughness parameter over all coarse grid points is  $\overline{n_{m,x}}=.053$ , which is 2.6 time greater than the high resolution value. Increasing the effective bottom friction is important for accurately

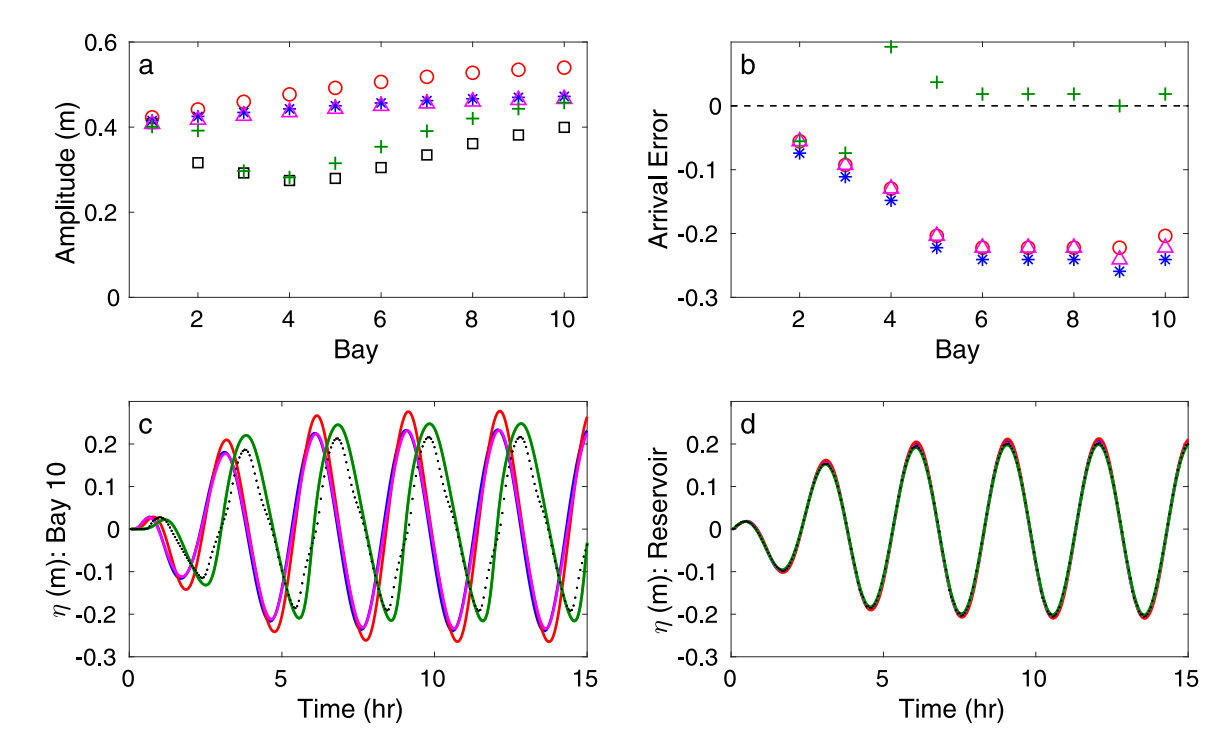


Fig. 10. Sea surface levels and timing of high tide events from the standard (red circles), Level 0 (blue stars), sub-Level 2 (magenta triangles), and Level 2 (green crosses) coarse simulations are compared with the high resolution simulation (black squares). (a) amplitude in each bay, where bay 1 is closest to the reservoir and bay 10 is farthest. (b) error in arrival time of high tide in each bay as a fraction of forcing period; the dashed black line indicates zero error. (c-d) Time series of surface elevation in the back bay (bay 10) and the reservoir.

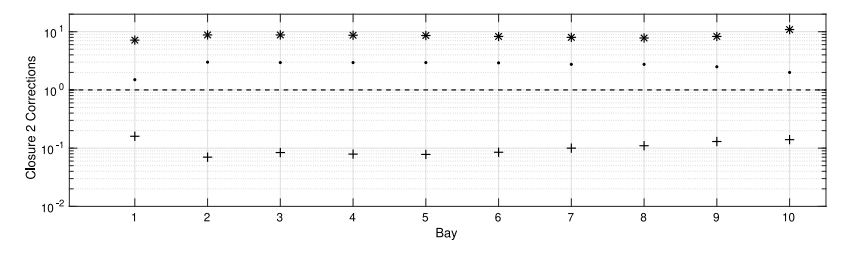


Fig. 11. Level 2 correction values imposed at each bay. The correction value for bay i is enforced at the bay i - channel i+1 boundary.  $C_{UU}$  (stars);  $C_{\eta,x}$  (crosses);  $n_{\eta x}/n$  (dots).

capturing event timings in the bays far from the reservoir, as well as lowering amplitudes in the back bays. Similarly, a large correction coefficient  $\overline{C_{UU}}=8.5$  is required in the convective term to account for the high velocity in the channel. The sea surface gradient on the other hand requires a reduction by approximately a factor of 10;  $\overline{C_{\eta,x}}=0.10$ . Note the surface gradient and convective corrections increased the accuracy of amplitudes. However, the overestimation of amplitude by the Level 2 closure suggests that the simple methodology used here: i.e. choosing one closure value that is independent of water level, may be too simplistic.

## 3.2.4. Level 2: Robustness

The sensitivity of Level 2 closure corrections to forcing frequency is tested by varying the forcing periods to  $T=1.5,\,2,\,3,\,6$  and 12 h, but using the same correction coefficients as were found for T=3 h. Fig. 12 plots the amplitude in the back bay against the forcing period for the different cases. As the frequency increases, the deviation in amplitude from the high resolution solution also increases for the standard and Level 0 methods (see Fig. 12(a)), while the Level 2 closure is considerably more accurate. Similarly, the errors in high tide arrival time increase with increasing forcing frequency for the standard and Level 0 methods (see Fig. 12(b)). Again, the Level 2 closure accounts for channel-scale physics that effectively delay the signal and therefore predict more accurately the timing of high tide events for

higher frequencies. Sub-Level 2 simulations (without surface gradient corrections) give results that are much worse than with full Level 2, almost certainly because of the large differences in surface gradients between wide bays and narrow channels. At low frequencies, all coarse methods provide accurate representation of sea surface evolution.

Fig. 12 (c–d) shows the time series of surface elevation in the back bay for the longest (12 h) and shortest (1.5 h) forcing periods. Using a 12 h period, all coarse simulation methods match the high resolution run. Using a higher forcing frequency, the errors in both amplitude and arrival time increase for the standard and Level 0 methods, thus suggesting the need for significant correction of the momentum equation. Fig. 12 shows the Level 2 closure can accurately approximate this correction for all tested forcing frequencies and that the coefficients needed for such corrections are relatively independent of frequency. Hence, this suggests that if the appropriate correction coefficients can be found, they could provide a robust model not only for the case where they are based on but also over more general conditions.

## 3.3. Complex test: Buttermilk bay

In this section, the subgrid system is applied to a more realistic simulation of flooding cycles at Buttermilk Bay, Massachusetts, USA (41.760N, 70.620W) (see Fig. 13). This multi-bay system has a main bay connected by a very narrow channel to a secondary bay (Little

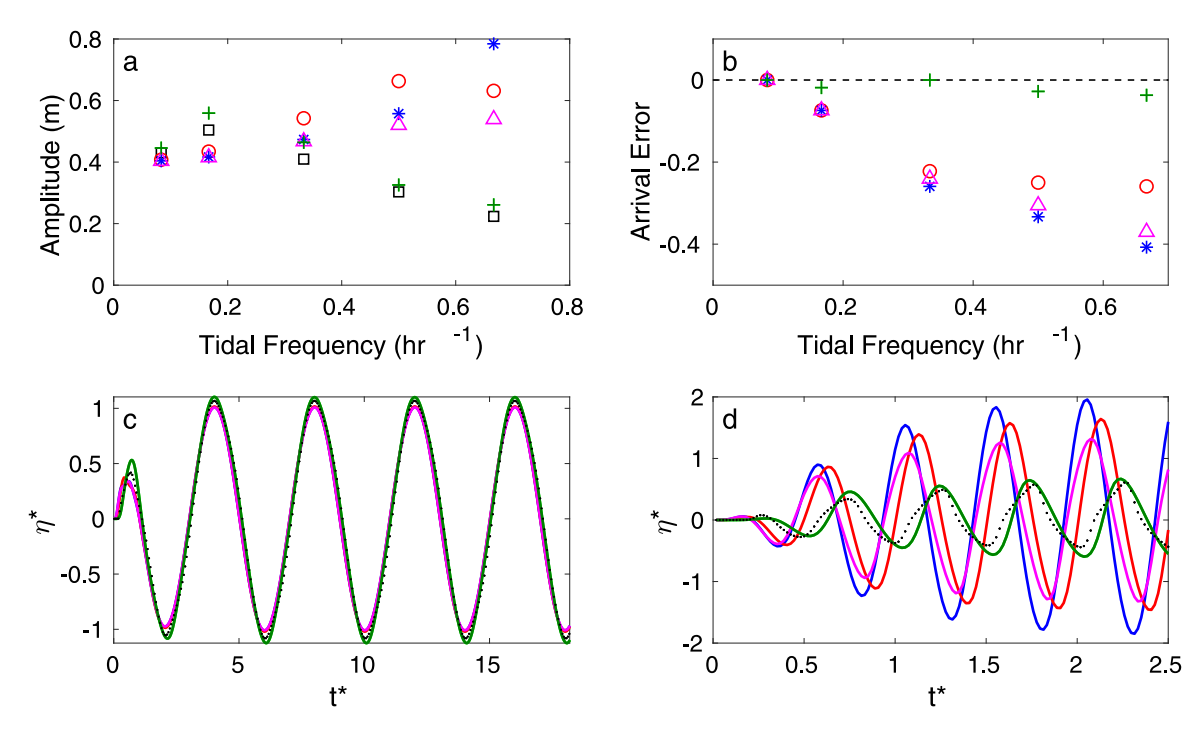


Fig. 12. Bay-channel simulation with varying forcing frequencies. High resolution runs (black square); coarse simulations using the standard solution (red circles), Level 0 (blue stars) and Level 2 (green crosses), sub-Level 2 (magenta triangles). (a) Back bay water surface amplitudes vs forcing frequency; (b) the relative error in high tide arrival in the back bay; (c-d) Time series of surface elevation from all coarse simulations with the longest (12 h) and shortest forcing periods (1.5 h), respectively.

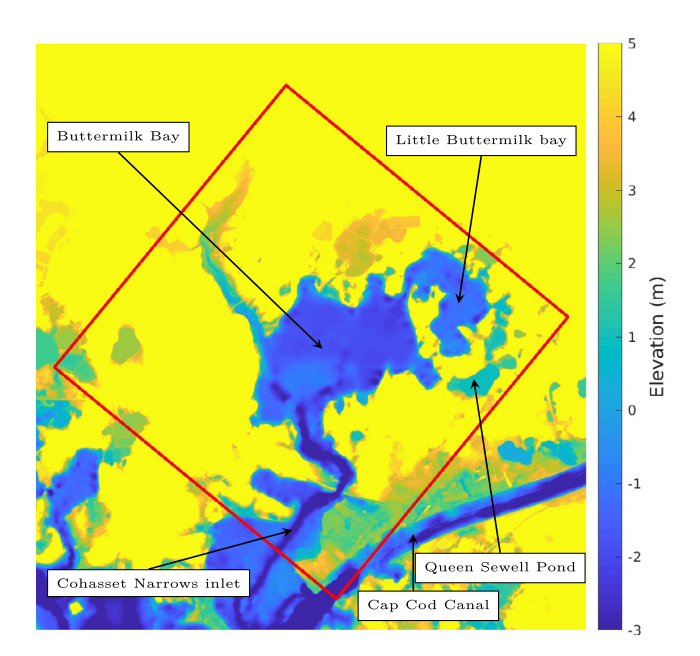


Fig. 13. LiDAR elevation map ff the Buttermilk bay area, Massachusetts, USA (41.760N,70.620W). The red box represents the computational domain.

Buttermilk Bay) that is quite difficult to simulate using standard techniques. A tertiary water body (Queen Sewell Pond) has a slightly higher elevation than the two main bays, but can be reached by high water levels.

The computational domain  $\Omega$  used here has dimensions 3584 m  $\times$  3584 m (red box in Fig. 13; see also Fig. 14). The simulation is driven at the southern boundary by the tide-like elevation boundary conditions (see Fig. 14). More specifically, the elevation boundary conditions

$$\eta = a_0 \tanh\left(\frac{2t}{T}\right) \cos(\omega t) \tag{31}$$

are imposed along (x, y = 0),  $2224 \le x \le 3234$ , the portion of the southern boundary close to the Cohasset Narrows inlet. Note that as the flow in the Cape Cod canal is not the main interest of this test, zero elevations are prescribed along the portion of boundaries intersecting the canal. In (31),  $a_0$  denotes the forcing amplitude,  $\omega$  the frequency, and  $T_r$  the ramping time. The test considered here simulates large semidiurnal tidal cycles and flow between the different bays. More precisely, the tidal frequency is set to  $\omega = 1.4544 \times 10^{-4} \text{ s}^{-1}$  and  $a_0 = 2 \text{ m}$ . This range is larger than the  $\sim 0.8$  m total combined semi-diurnal M2, S2, N2, and K2 tides (see Anon., 0000) in this area. Note that this unrealistically large tidal amplitude is intentionally employed in order to test the robustness of the subgrid system in dealing with filling and draining. The test considers neither wind nor atmospheric pressure forcing. All simulations are started from a quiescent initial state. The elevation forcing is gradually ramped from zero with the ramping time  $T_r = 0.25 \text{ day.}$ 

Level 0 and Level 1 closures are considered in the subgrid system. The momentum equations in the quasi-non-conservative forms are employed in the numerical calculations. Six computational coarse grids are used for intercomparison with resolutions  $\Delta x = \Delta y =$ (512, 256, 128, 64, 32, 16, 8) m. The staggered FD/FV solution with Casulli's subgrid wetting/drying (Casulli, 2009) computed on the 4 m grid is used as a reference solution (our numerical schemes with Level 0 closure is to large extent very similar to this FD/FV scheme). Here, the finer grids are obtained successively by dividing each grid cell into four uniform cells. In all subgrid calculations, 1 m LiDAR elevation data are used to describe the subgrid bathymetric depth (Danielson et al., 2018). A standard model, where the bathymetric depth in each cell is equal to an average of the LiDAR data over the cell, is also considered for comparison purposes. Fig. 15 illustrates the cellaveraged bathymetric depth of the area north of the Cohasset narrow on the grids of successively coarsening resolution. The resolution of the grid shown in Fig. 15(c) is 64 m, which is slightly coarser than the typical finest grid size used in the floodplains of state-of-the-art high-resolution storm surge models, such as ADCIRC (Tanaka et al., 2011; Hope et al., 2013). It can be noticed that a large amount of topographical detail is already lost at this level of resolution, and

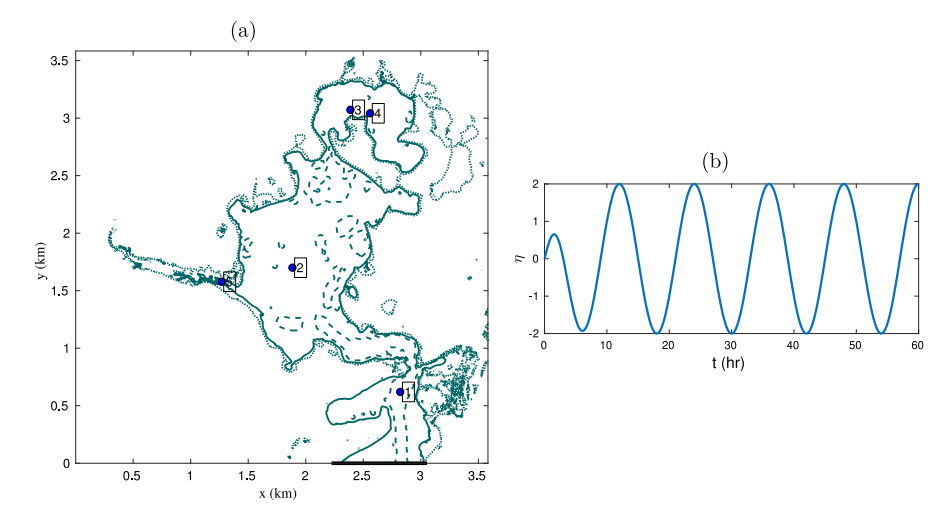


Fig. 14. Computational domain with three selected contours of bathymetric depth (contour lines: -2 m = -; 0 m; 2 m  $\cdots$ ). The location where the elevation boundary conditions are imposed along the segment  $2224 \le x \le 3234$ , y = 0 and is illustrated by a thick black segment. (b) Time-dependent elevation boundary values.

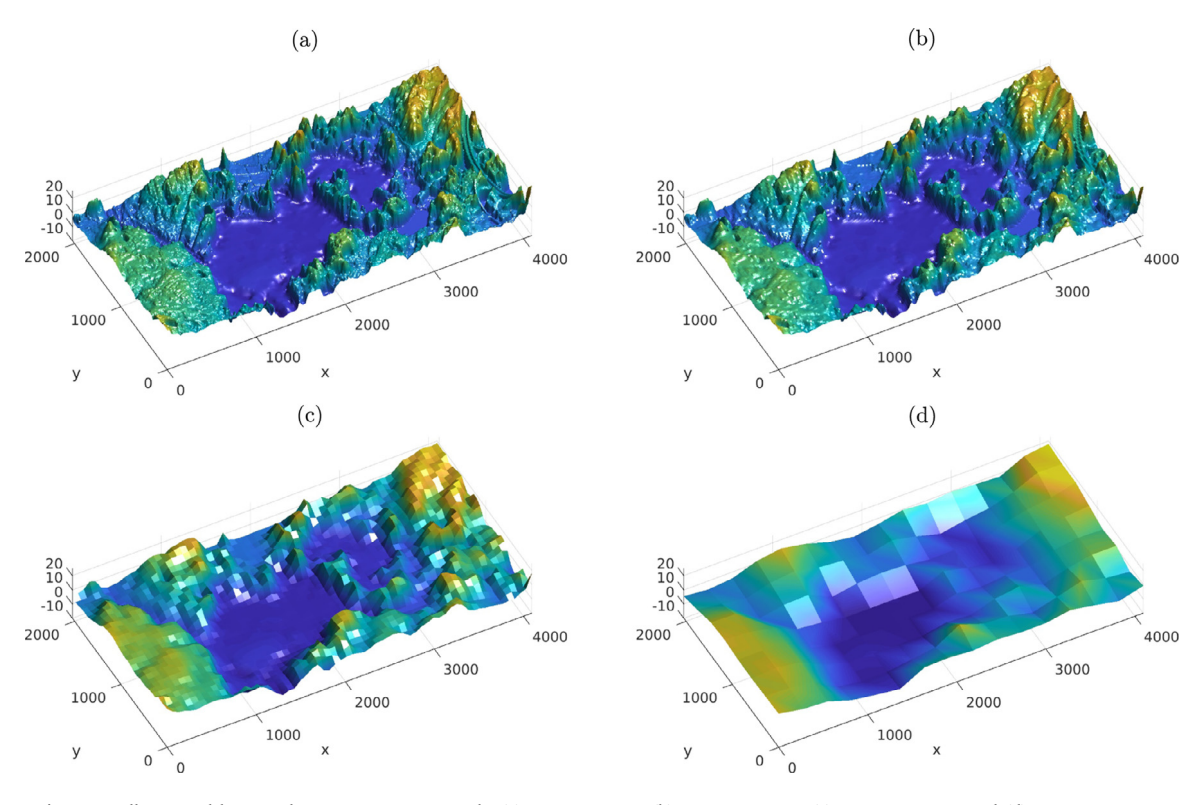


Fig. 15. Cell-averaged bottom elevations on various grids: (a)  $\Delta x = \Delta y = 8$  m, (b)  $\Delta x = \Delta y = 16$  m, (c)  $\Delta x = \Delta y = 64$  m, and (d)  $\Delta x = \Delta y = 256$  m.

further loss of detail can be clearly observed as the grid resolutions are further coarsened.

Figs. 16–18 show respectively the surface elevation of the wet area computed on the grids of 8, 64, 256 m resolution at three specific times in which the tide at the boundary is rising. In these figures, plots on the left column show the results from the standard model and the right column show the results from the subgrid model with Level 0 closure. It is noted that cells in the standard model are either wet or dry while in the subgrid model the cells can be partially wet.

When the high resolution 8 m grid is used, i.e. when the topographical features are sufficiently resolved, the results from the standard model and the subgrid model are in very good agreement (see Fig. 16). As can be seen in Fig. 18, the coarse grid 256 m solution of the standard model completely fails to capture the connections between the bays due to the loss of topographical details of the averaged topography. It can

be clearly observed that the subgrid model is indeed able to capture all connections between the inlet, main bay and back bay in the coarse grid solution. In addition, the passages of water through the small hydroconnectivity features, i.e. a brook at the northwest of the main bay and a small channel on the southern end of the back bay, are clearly present in the subgrid solution. For the 64 m grid (see Fig. 17), although the connection between the main bay and back bay exists in the solution of the standard model, it is clearly insufficient as indicated by the time lag of the response in the back bay. Although not shown in this figure, it is noted that the numerical solutions of the subgrid model with Level 1 closure are qualitatively and quantitatively very similar to the solution of the Level 0 closure.

The time series of the surface elevation are recorded at different locations. Figs. 19–22 plot the time series at stations marked by blue dots in Fig. 14(a). In these figures, the top panel shows the standard

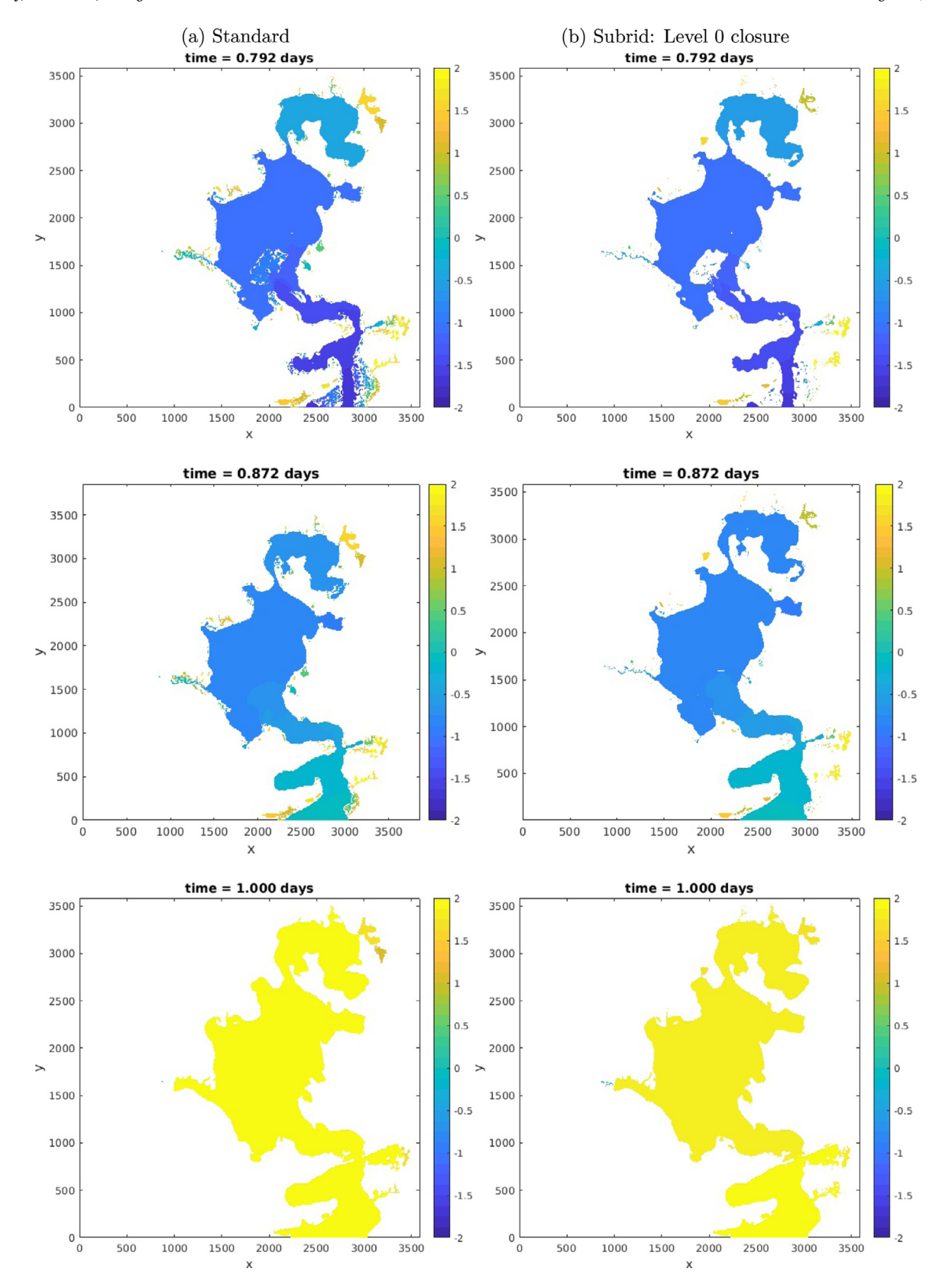


Fig. 16. Solutions computed on grid of  $\Delta x = \Delta y = 8$  m at different time levels. (a) standard model; (b) subgrid model with Level 0 closure.

solution and the bottom panel shows the subgrid solution with Level 0 closure computed on various grids. Note that because the results from Level 1 closure are virtually identical to that of Level 0, they are omitted from the plots. From these figures, it can be clearly noticed

that, when using the same resolution, coarse grid solutions obtained from the subgrid model are always in better agreement with the 4 m reference solution than the standard model. Indeed, flow does not reach the main bay and Little Buttermilk Bay when coarse grids are used in

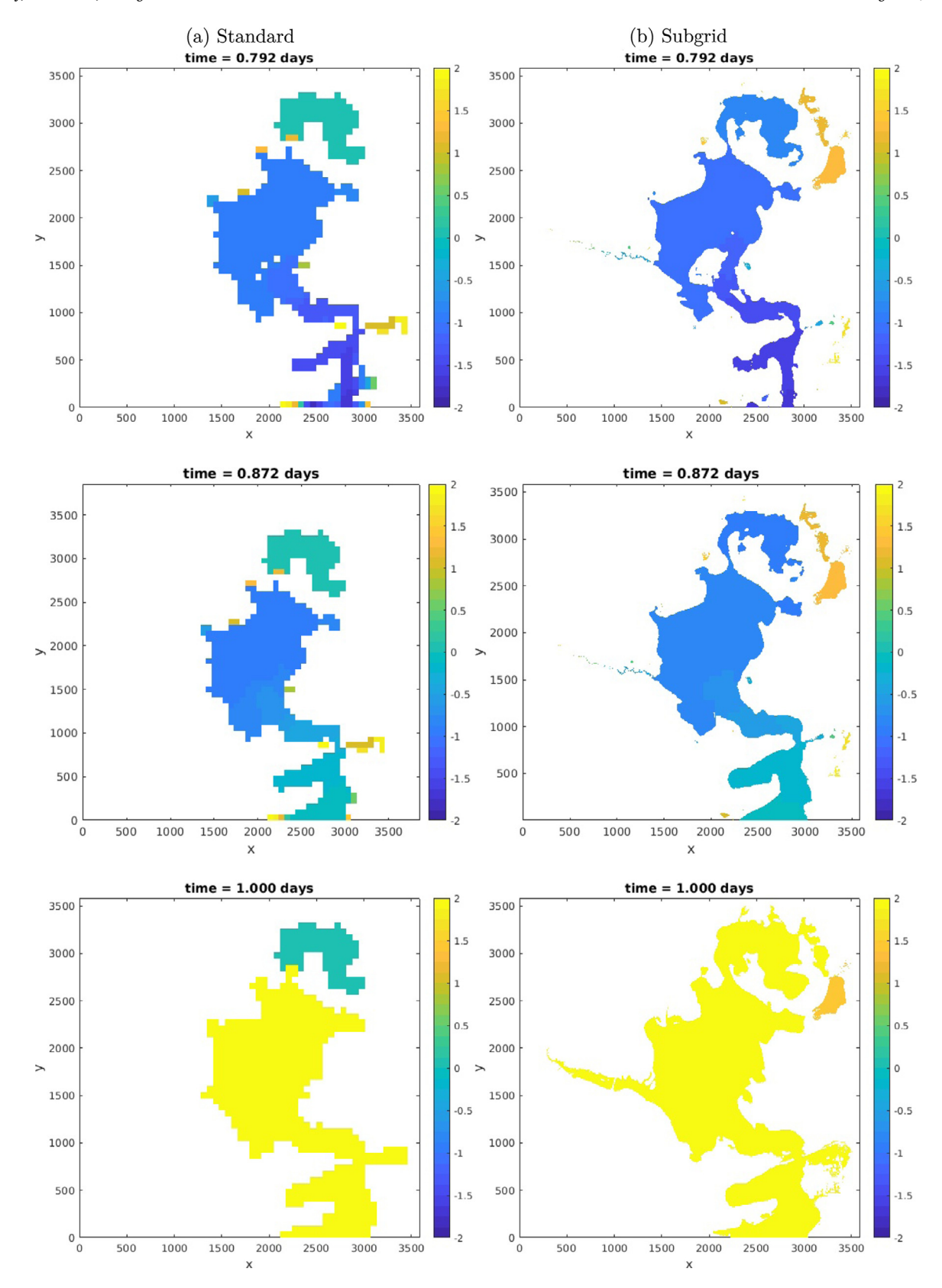


Fig. 17. Solutions computed on grid of  $\Delta x = \Delta y = 64$  m at various time level. (a) conventional model; (b) subgrid model with level 0 closure.

the standard solution. At these locations, a much higher resolution is required in the standard model in order to obtain numerical results that are comparable to that of the coarse grid subgrid model. Note that flow from the inlet enters Buttermilk Bay and its back bay through

the channels; both the subgrid and standard solutions show an increase in grid sensitivity at the stations in the secondary bays in comparison to those at Station 1. However, the subgrid model is significantly less sensitive to grid resolution than the standard model.

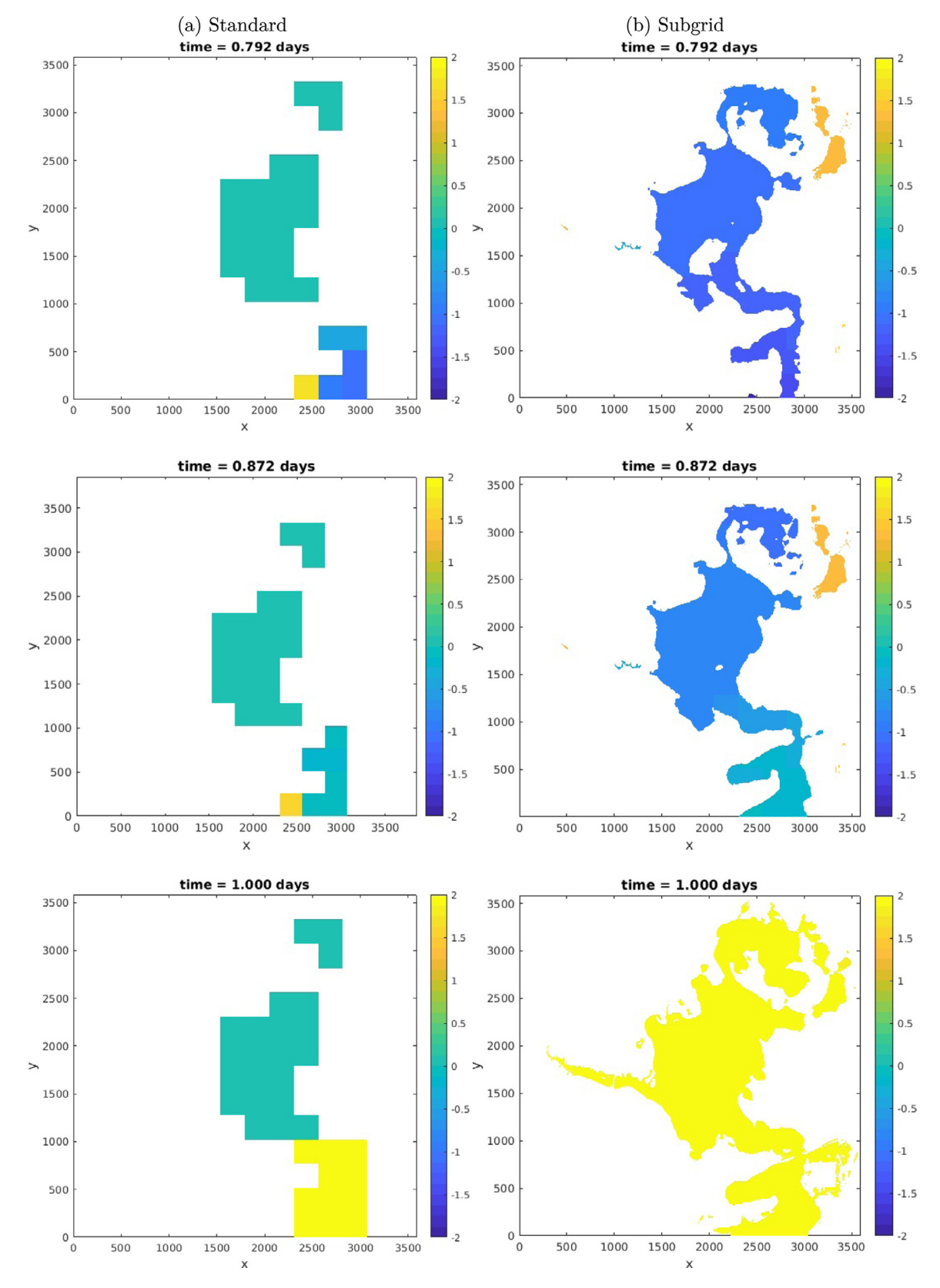
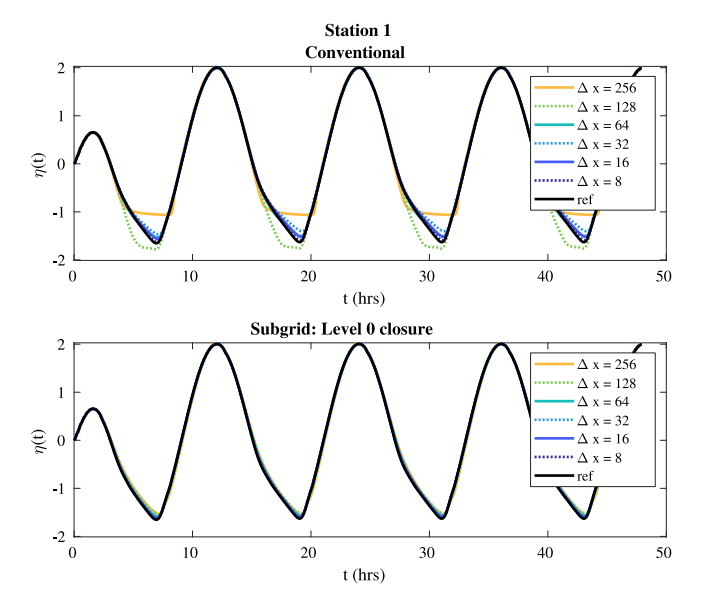


Fig. 18. Solutions computed on grid of  $\Delta x = \Delta y = 256$  m at various time level. (a) conventional model; (b) subgrid model with Level 0 closure.

The usual Root-Mean-Square (RMS) errors over one cycle are given by

$$E(\mathbf{x}) = \sqrt{\frac{1}{N} \sum_{i=1}^{N} \left( \eta(\mathbf{x}, t^i) - \eta_{\text{ref}}(\mathbf{x}, t^i) \right)^2}, \quad t^i = i\delta t + T_a$$
(32)

where N denotes the number of samples over one cycle with  $\delta t = 5$  min sampling size and  $T_a = 1$  day denotes an offset constant. These are given in Table 1 (a–c) for the standard, Level 0 closure, and Level 1 closure solutions, respectively. For the same grid resolution, the RMS



**Fig. 19.** Time series of surface elevation  $\eta(t)$  at Station 1 located near Cohasset Narrows inlet.

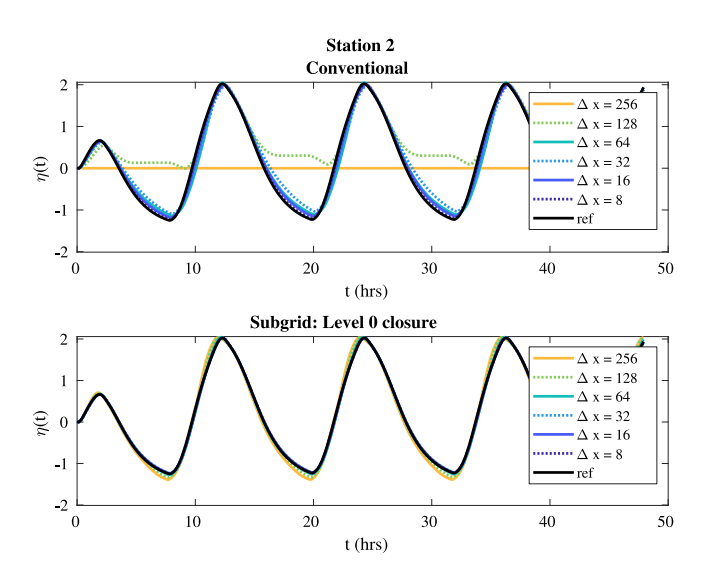


**Fig. 20.** Time series of surface elevation  $\eta(t)$  at Station 2 located in the Buttermilk bay.

errors in the subgrid solution are at worst comparable to one order of magnitude lower than those of the standard solution at all stations. As qualitatively observed in the previous plots, the RMS errors in the coarse grid solution from the subgrid model are directly comparable to those of the standard solution computed on the higher resolution grid. For example, at Station 3, the subgrid Level 0 closure solution on 256 m grid is roughly comparable to the standard solution on 32 m to 64 m grids. At Station 5, which is located in the wetting/drying areas, the subgrid solution is comparable to the standard solution on 8 m to 16 m grids, which are even finer than those seen in Station 3. The results demonstrate the potential cost savings from employing the subgrid model, as reasonable results may be obtained with significantly lower degrees of freedom (approximately one to two orders of magnitude for this particular test). In comparison to the reference solution used, errors in the Level 1 closure solution are in overall slightly higher than those of the Level 0 closure solution; the Level 1 closure solution shows slightly lower error levels at some grid resolutions especially at Station 1. This is somewhat unexpected, as it would be surmised that Level 1

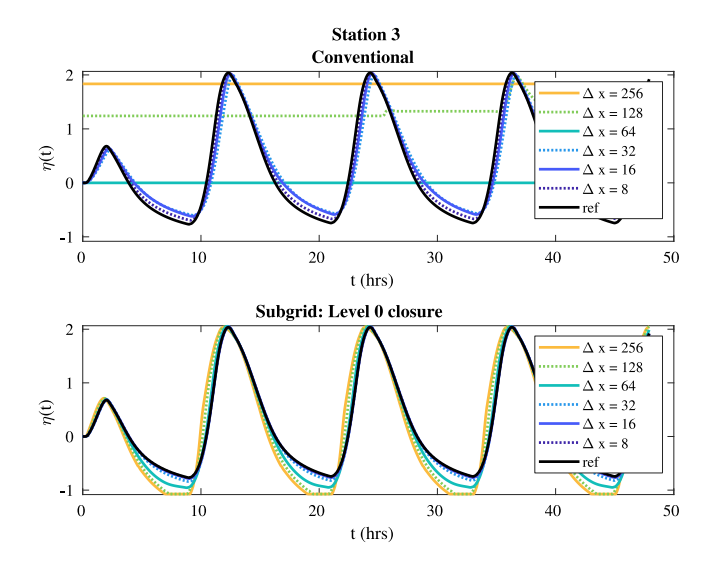


**Fig. 21.** Time series of surface elevation  $\eta(t)$  at Station 3 located in the Little Buttermilk Bay.

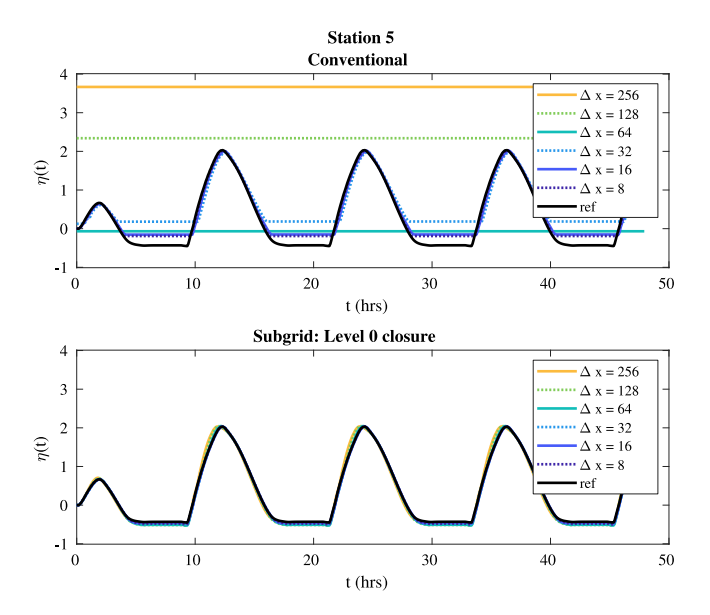


Fig. 22. Time series of surface elevation  $\eta(t)$  at Station 5.

would be more accurate. The reasons for the difference appear to be because, for larger grid sizes, a single cell near the connections can contain both part of the large bay and a narrow channel, much like in Section 3.2.3. Thus, Level 1 assumptions are not necessarily more appropriate. A second reason arises from artificial connectivity induced by two separate water bodies without connectivity appearing in some of the largest grid cells for both Levels 0 and 1. As it is now, the system assumes that these bodies are connected at the subgrid level, but this is not necessarily true. Nevertheless, the differences between the error levels in the Level 1 and 0 closure solution are negligibly small.

Lastly, it is worthwhile to mention that at these stations, the numerical rates of convergence of both Level 0 and Level 1 closure subgrid models range approximately from 0.5 to 1 (i.e.  $E_s \sim O(h^p)$ ,  $p \approx 0.5-1.0$ ). The rates are within the range of values to be generally expected in our numerical schemes since they are based on the use of the first order upwind scheme and a fixed mesh solution technique in dealing with the problem of wetting/drying areas.

Table 1 Buttermilk bay test case: RMS surface elevation errors  $E(x_s)$  (m) at various locations in: (a) the standard solution, (b) subgrid solution with Level 0 closure, and (c) subgrid solution with Level 1 closure.

(a) Standard solu	tion				
Grid size (m)	Station 1	Station 2	Station 3	Station 4	Station 5
512	2.5641	1.2082	1.1968	1.1974	9.0879
256	0.2004	1.1318	1.7982	1.0013	3.3728
128	0.1685	0.7983	1.4457	1.4585	2.1253
64	0.0385	0.1723	0.9981	1.0013	1.0284
32	0.0867	0.2309	0.2912	0.2953	0.4262
16	0.0451	0.0996	0.2056	0.2085	0.1915
8	0.0217	0.0433	0.0971	0.0985	0.1554
(b) Subgrid solut	ion with Level	0 closure			
Grid size (m)	Station 1	Station 2	Station 3	Station 4	Station 5
512	0.1139	0.3216	0.6156	0.5963	0.2720
256	0.0737	0.1229	0.3974	0.3809	0.0882
128	0.0583	0.0751	0.3013	0.2846	0.0766
64	0.0354	0.0331	0.1537	0.1518	0.0534
32	0.0254	0.0303	0.0453	0.0449	0.0326
16	0.0196	0.0245	0.0192	0.0207	0.0247
8	0.0100	0.0097	0.0086	0.0088	0.0301
(c) Subgrid solut	ion with Level	1 closure			
Grid size (m)	Station 1	Station 2	Station 3	Station 4	Station 5
512	0.1406	0.3527	0.6278	0.6078	0.2806
256	0.0667	0.1546	0.4281	0.4093	0.1063
128	0.0520	0.0866	0.3302	0.3113	0.0804
64	0.0334	0.0352	0.1666	0.1646	0.0668
32	0.0244	0.0287	0.0507	0.0499	0.0376
16	0.0196	0.0247	0.0206	0.0221	0.0268
8	0.0101	0.0099	0.0092	0.0096	0.0329

### 4. Discussion and conclusions

When compared to standard shallow water solutions, it is clear that the use of subgrid corrections derived by a formal averaging process allows increased accuracy in complex shore regions when using lower resolution simulations. However, simulation accuracy depends greatly on the form of closures, and more complex scenarios may require more complex closures. Most of the closure terms derived by the averaging process might have been expected from intuition and some have already been implemented by other researchers; however, corrections to the gradient of mean water surface elevations shown in Eqs. (20)–(21) are less obvious but appear quite necessary in situations where flow characteristics change strongly within an averaging volume. Determination of closure coefficients remains a challenging task, and much work will be required to investigate general closure methodologies. However, the repeating bay-channel test case showed that even in systems that display complex geometries and have non-linear effects, a simple coefficient can still effectively capture much of the subgrid physics at play and significantly improve model performance. Anisotropy of friction and spatial variability of surface elevation gradients is another area where further research is needed. Tensorial Manning's coefficients have been used by inland flooding researchers (Viero and Valipour, 2017) but their application to general inhomogeneous topographies is not yet a solved problem.

One aspect of the subgrid system that was not addressed but is very important in many coastal regions is flow connectivity through an averaging area. The work presented here does not yet consider whether flow at the boundaries has a path to reach other boundaries of a grid cell or whether it is blocked by land. In some regions, including the Buttermilk Bay simulations, not accounting for these non-continuous flow paths may be a limiting factor for simulation accuracy, and as seen in Fig. 1. Very recently, Casulli (2019) addressed this issue by "cloning" cells and edges based on connectivity, effectively introducing additional degrees of freedom into a single grid location. Corrections such as this appear to be necessary when a single degree of freedom is insufficient.

Flow connectivity is an important area of research that continues to be actively investigated.

All tests considered here were conducted on relatively small regular grids using a code written specifically for the subgrid system. Most typical storm surge and circulation simulations use much larger grids and may have very different grid properties. Efforts are underway to incorporate the subgrid corrections introduced here into more widely-used and available models that have a greater impact on the field and will be reported on in the future.

#### Acknowledgments

Work here was funded under National Science Foundation, USA grants ICER 1664040 and 1664037, and through a grant from the Joint Airborne Lidar Bathymetry Technical Center of Expertise (JALBTCX), USA through a subcontract with Optimal Geo. TS is supported by the National Science Foundation, USA Graduate Research Fellowship under Grant No. DGE-1841556. Their support is gratefully acknowledged.

## Appendix A. Quasi-non-conservative form of subgrid equations

Non-conservative forms of shallow water-like equations are useful for many numerical schemes. The most obvious subgrid solution is to perform averaging on the nonconservative form directly and then to develop closures. This naive methodology proves suboptimal, as Whitaker averaging in this form generates several difficulties to close boundary integral terms that disappear in the conservative forms because of the zero depth (and thus momentum) at the wet–dry boundary. An alternate methodology that removes these forms is to begin with (27)–(28) and use the product rule to expand the third and fourth terms on the left hand side of (27) and (28) to arrive at

$$\langle H \rangle_{G} \frac{\partial \langle U \rangle}{\partial t} + \langle U \rangle \nabla \cdot \left[ ((C_{UU} - 1) \langle U \rangle, (C_{UV} - 1) \langle V \rangle) \langle H \rangle_{G} \right]$$

$$+ C_{UU} \langle U \rangle \langle H \rangle_{G} \frac{\partial \langle U \rangle}{\partial x} + C_{UV} \langle V \rangle \langle H \rangle_{G} \frac{\partial \langle U \rangle}{\partial y}$$

$$= -gC_{\eta,xx} \langle H \rangle_{G} \frac{\partial \langle \eta \rangle}{\partial x} - g \langle H \rangle_{G} C_{\eta,xy} \frac{\partial \langle \eta \rangle}{\partial y}$$

$$-\phi |\langle U \rangle| \left[ c_{M,fxx} \langle U \rangle + c_{M,fxy} \langle V \rangle \right]$$

$$+\phi \frac{\langle \tau_{sx} \rangle_{W}}{\rho} - \frac{\langle H \rangle_{G}}{\rho} \frac{\partial P_{A}}{\partial x} - f_{c} \langle V \rangle \langle H \rangle_{G}$$

$$+ \frac{1}{\rho} \frac{\partial}{\partial x} \left( \langle H \rangle_{G} \mu_{t} \frac{2\partial \langle U \rangle}{\partial x} \right) + \frac{1}{\rho} \frac{\partial}{\partial y} \left( \langle H \rangle_{G} \mu_{t} \left( \frac{\partial \langle U \rangle}{\partial y} + \frac{\partial \langle V \rangle}{\partial x} \right) \right)$$
 (33)

$$\begin{split} &\langle H \rangle_{G} \frac{\partial \langle V \rangle}{\partial t} + \langle V \rangle \nabla \cdot \left[ \left( (C_{VU} - 1) \langle U \rangle, (C_{VV} - 1) \langle V \rangle) \langle H \rangle_{G} \right] \\ &+ C_{VU} \langle U \rangle \langle H \rangle_{G} \frac{\partial \langle V \rangle}{\partial x} + C_{VV} \langle V \rangle \langle H \rangle_{G} \frac{\partial \langle V \rangle}{\partial y} \\ &= -g C_{\eta,yx} \langle H \rangle_{G} \frac{\partial \langle \eta \rangle}{\partial x} - g C_{\eta,yy} \langle H \rangle_{G} \frac{\partial \langle \eta \rangle}{\partial y} - \\ &- \phi |\langle U \rangle | \left[ c_{M,fyx} \langle U \rangle + c_{M,fyy} \langle V \rangle \right] \\ &+ \phi \frac{\langle \tau_{sy} \rangle_{W}}{\rho} - \frac{\langle H \rangle_{G}}{\rho} \frac{\partial P_{A}}{\partial x} + f_{c} \langle U \rangle \langle H \rangle_{G} \\ &+ \frac{1}{\rho} \frac{\partial}{\partial x} \left( \langle H \rangle_{G} \mu_{t} \left( \frac{\partial \langle U \rangle}{\partial y} + \frac{\partial \langle V \rangle}{\partial x} \right) \right) + \frac{1}{\rho} \frac{\partial}{\partial y} \left( \langle H \rangle_{G} \mu_{t} \frac{2\partial \langle V \rangle}{\partial y} \right) \end{split} \tag{34}$$

Note that the above forms offer convenience in numerical realization as the differences between the implementations of the quasi-conservative and quasi-non-conservative are only in the discretization schemes for the advection terms (see Appendix B for more details). Note that the quasi-non-conservative forms that resemble more to the conventional non-conservative forms can be obtained by dividing both sides of the above equations by the grid-average depth.

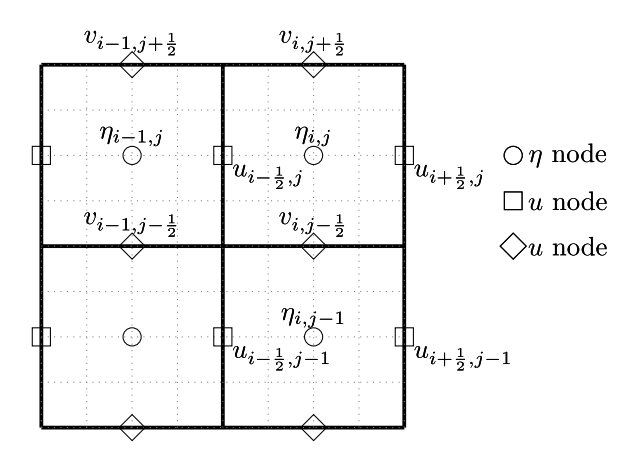


**Fig. 23.** Staggered grid. The surface elevation is located in the cell center; the horizontal velocity u at the midpoint of the cell vertical edges; the vertical velocity v at the midpoint of the cell horizontal edges.

### Appendix B. FD Scheme on structured staggered grid

This section describes finite difference schemes on a staggered grid used in numerical discretization of the governing equations (15),(27), and (28). These finite difference schemes are based in large part on adaptations of the numerical schemes presented in Casulli (1990, 2009), Stelling and Duinmeijer (2003), Volp et al. (2013) to accommodate the proposed subgrid governing equations. Note that although the mass equations (15) and (16) are equivalent (when V is defined by (9)); (15) is chosen since it leads to a preferable property of mass conservation at the discrete level. The terms associated with cross-term closure coefficients  $C_{\eta,xy}$ ,  $C_{\eta,yx}$ ,  $c_{M,f,xy}$ ,  $c_{M,f,yx}$  in the averaged momentum equations are excluded in this study; they will be implemented in a future study.

Here, the standard 2D Arakawa C grid is adopted. The unknown flow variables  $\langle \eta \rangle$ ,  $\langle U \rangle$ , and  $\langle U \rangle$  are placed at the cell-center, and at the midpoint of the vertical and horizontal cell edges, respectively (see Fig. 23). The mass (15) and the *x*-momentum (27), and the *y*-momentum (28) are discretized at the nodes associated with the discrete variables  $\langle \eta \rangle$ ,  $\langle U \rangle$ , and  $\langle V \rangle$ , respectively. To keep the notation simple,  $\eta$ , U, V, and V will be used to refer to the averaged variables  $\langle \eta \rangle$ ,  $\langle U \rangle$ ,  $\langle U \rangle$ , and  $\langle V \rangle$ , respectively. The precise notation will be used when it is not clear from context. The control volumes

$$\begin{split} &\Omega_{\eta_{i,j}} = [x_{i-\frac{1}{2}}, x_{i+\frac{1}{2}}] \times [y_{j-\frac{1}{2}}, y_{j+\frac{1}{2}}], \quad \Omega_{u_{i-\frac{1}{2},j}} = [x_{i-1}, x_i] \times [y_{j-\frac{1}{2}}, y_{i,j+\frac{1}{2}}] \\ &\Omega_{v_{i,j-\frac{1}{2}}} = [x_{i-\frac{1}{2}}, x_{i+\frac{1}{2}}] \times [y_{j-1}, y_{i,j+1}]. \end{split}$$

are assigned to the flow variables  $\eta_{i,j}, u_{i-\frac{1}{2}}, j$ , and  $v_{i,j-\frac{1}{2}}$ , respectively. The averaging area  $A_G$  is assumed to be identical to the grid size (the control volume size). For a given  $\eta$  and bathymetric depth h(x) (of arbitrarily fine resolution), the value of the averaged water depth at each node is evaluated from the formula (9) with the integration defined over its associated control volume. (See Fig. 24.)

## B.0.1. Continuity discretization

A semi-implicit finite difference discretization of the continuity equation (15) for a cell (i, j)

$$\frac{V_{i,j}(\eta_{i,j}^{n+1}) - V_{i,j}(\eta_{i,j}^{n})}{\Delta t} + \frac{u_{i+\frac{1}{2},j}^{n+1} H_{i+\frac{1}{2},j}^{n} - u_{i-\frac{1}{2},j}^{n+1} H_{i-\frac{1}{2},j}^{n}}{\Delta x} + \frac{v_{i,j+\frac{1}{2}}^{n+1} H_{i,j+\frac{1}{2}}^{n} - v_{i,j-\frac{1}{2}}^{n+1} H_{i,j-\frac{1}{2}}^{n}}{\Delta x} + \frac{v_{i,j+\frac{1}{2}}^{n+1} H_{i,j+\frac{1}{2}}^{n} - v_{i,j-\frac{1}{2}}^{n+1} H_{i,j-\frac{1}{2}}^{n}}{\Delta x} = 0$$

is considered. This scheme is a result of using the Euler backward in time discretization with the grid-averaged total water depth H from

the current time level. By multiplying the above equation by  $\Delta x \Delta y$ , one has

$$\frac{V_{i,j}(\eta_{i,j}^{n+1}) - V_{i,j}(\eta_{i,j}^{n})}{\Delta t} + u_{i+\frac{1}{2},j}^{n+1} A_{i+\frac{1}{2},j}^{n} - u_{i-\frac{1}{2},j}^{n+1} A_{i-\frac{1}{2},j}^{n} 
+ v_{i,j+\frac{1}{2}}^{n+1} A_{i,j+\frac{1}{2}}^{n} - v_{i,j-\frac{1}{2}}^{n+1} A_{i,j-\frac{1}{2}}^{n} = 0,$$
(35)

a form reminiscent of the FV scheme, where  $V_{i,j}$  is the water volume in the cell,  $A_{i+\frac{1}{2},j}^{n+1}=H_{i+\frac{1}{2},j}^{n}\Delta y$  and  $A_{i,j+\frac{1}{2}}^{n+1}=H_{i,j+\frac{1}{2}}^{n}\Delta x$ . The grid-averaged water height  $H_{i+\frac{1}{2},j}$  is determined by

$$H_{i+\frac{1}{2},j} = \frac{1}{\Delta x \Delta y} \int_{\Omega_{u}} H dx$$

$$= \frac{1}{\Delta x \Delta y} \left( \int_{x_{i}}^{x_{i+1/2}} \int_{y_{i-1/2}}^{y_{i+1/2}} H(\eta_{i,j}) dx dy + \int_{x_{i+1/2}}^{x_{i+1}} \int_{y_{i-1/2}}^{y_{i+1/2}} H(\eta_{i+1,j}) dx dy \right).$$
(36)

The grid-average at the v-node  $H_{i,j+\frac{1}{2}}$  is defined in the same manner. It is noted that the formula (35) is written for any cell having at least one wet edge. The edge is considered wet when the wet cross-section area of such edge is greater than a given, small positive tolerance. More precisely, the edge associated with  $u_{i+\frac{1}{8},j}$  is considered wet when

$$\int_{y_{i-\frac{1}{2}}}^{y_{j+\frac{1}{2}}} H(\eta_{i+\frac{1}{2},j}) dy > \varepsilon$$

where

$$\eta_{i+\frac{1}{2},j} = \frac{\eta_{i,j} + \eta_{i+1,j}}{2}.$$

## B.O.2. Momentum discretization

For simplicity of presentation, the x- and y-directed bottom stresses  $\tau_{bx}$  and  $\tau_{by}$  are written as

$$\left\langle \frac{\tau_{bx}}{\rho} \right\rangle_{W} = \gamma \left\langle U \right\rangle, \quad \left\langle \frac{\tau_{by}}{\rho} \right\rangle_{W} = \gamma \left\langle V \right\rangle$$

Below, the discretization of the x-momentum equation (27) is described. A semi-implicit finite difference scheme on the u-node is given by

$$H_{i+\frac{1}{2}}^{n} \frac{u_{i+\frac{1}{2},j}^{n+1} - u_{i+\frac{1}{2},j}^{n}}{\Delta t} + F_{i+\frac{1}{2},j}^{n} = -gH_{i+\frac{1}{2},j}^{n} C_{\eta,(i+\frac{1}{2},j)} \frac{\eta_{i+1,j} - \eta_{i,j}}{\Delta x} - \gamma_{i+\frac{1}{2},j} u_{i+\frac{1}{2},j}^{n+1}$$
(37)

where

$$F_{i+\frac{1}{2},j}^{n} = -u_{i+\frac{1}{2},j} \left( \frac{Q_{E}^{u} - Q_{W}^{u}}{\Delta x} + \frac{Q_{N}^{v} - Q_{S}^{v}}{\Delta y} \right) + \frac{C_{UU,E} Q_{E}^{u} u_{E}^{n} - C_{UU,W} Q_{W}^{u} u_{W}^{n}}{\Delta x} + \frac{C_{UV,N} Q_{N}^{v} u_{N}^{n} - C_{UV,S} Q_{S}^{v} u_{S}^{n}}{\Delta y}$$
(38)

is the discretization formula of the advection term. Note that, in this discretization formula, the bottom friction and the surface gradient terms are treated implicitly via the Euler-backward scheme while the advection terms are treated explicitly through the Euler-forward scheme.

In (38),  $Q_E^u$ ,  $Q_W^u$  represent the x-directed mass fluxes at the east and west edges of the control volume  $\Omega_u$  while  $Q_N^v$  and  $Q_S^v$  denote the y-directed mass fluxes at the north and south edges. They are evaluated through the following formula

$$Q_E^u = \frac{u_{i+\frac{1}{2},j}^n H_{i+\frac{1}{2},j}^{n-1} + u_{i+\frac{3}{2},j}^n H_{i+\frac{3}{2},j}^{n-1}}{2}, \ Q_W^u = \frac{u_{i-\frac{1}{2},j}^n H_{i-\frac{1}{2},j}^{n-1} + u_{i+\frac{1}{2},j}^n H_{i+\frac{1}{2},j}^{n-1}}{2}$$

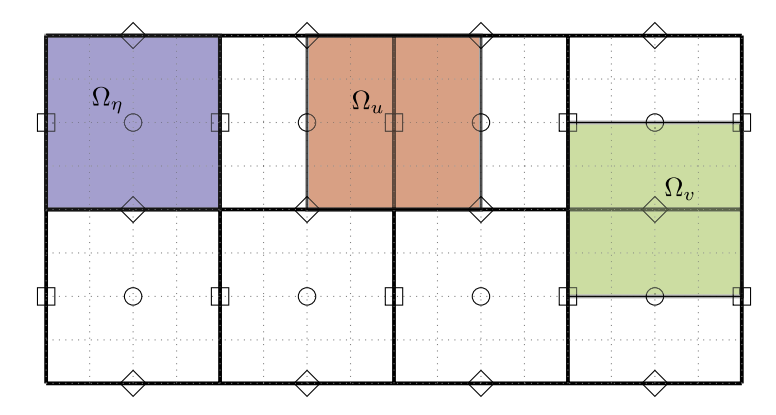


Fig. 24. Control volume associated with each flow variable.  $\Omega_{\eta}$  control volume for discretizing the continuity equation;  $\Omega_{u,v}$ -control volume for discretizing the x- and y-momentum equations.

$$\begin{split} Q_N^v &= \frac{v_{i,j+\frac{1}{2}}^n H_{i,j+\frac{1}{2}}^{n-1} + v_{i+1,j+\frac{1}{2}}^n H_{i+1,j+\frac{1}{2}}^{n-1}}{2}, \\ Q_S^v &= \frac{v_{i,j-\frac{1}{2}}^n H_{i,j-\frac{1}{2}}^{n-1} + v_{i+1,j-\frac{1}{2}}^n H_{i+1,j-\frac{1}{2}}^{n-1}}{2}. \end{split}$$

The velocities  $u_E$ ,  $u_W$ ,  $u_N$ , and  $u_S$ , which are the x-directed velocity along the east, west, north, and south edges of the control volume  $\Omega_u$ , respectively, are determined by a first order upwind scheme with an upwind direction determined by a sign of the flow  $Q_v$ , more precisely

$$u_{E} = \begin{cases} u_{i+\frac{1}{2},j}, & Q_{E}^{u} > 0 \\ u_{i+\frac{3}{2},j}, & Q_{E}^{u} < 0 \end{cases}, \quad u_{W} = \begin{cases} u_{i-\frac{1}{2},j}, & Q_{W}^{u} > 0 \\ u_{i+\frac{1}{2},j}, & Q_{W}^{u} < 0 \end{cases},$$

$$u_{N} = \begin{cases} u_{i+\frac{1}{2},j}, & Q_{N}^{v} > 0 \\ u_{i+\frac{1}{2},j+1}, & Q_{N}^{v} < 0 \end{cases}, \quad u_{W} = \begin{cases} u_{i+\frac{1}{2},j-1}, & Q_{S}^{v} > 0 \\ u_{i+\frac{1}{2},j}, & Q_{S}^{v} < 0 \end{cases}.$$
(39)

It can be verified that when  $C_{UU}$  and  $C_{UV}$  are set to one, the discrete advection term is simply an upwind scheme. For example, if the flow direction is positive ( $Q_e > 0$ ), the discrete advection term at the  $u_{i+\frac{1}{2},j}$ -node corresponds to

$$F_{i+\frac{1}{2},j}^{n} = Q_{W}^{u} \frac{u_{i+\frac{1}{2},j} - u_{i-\frac{1}{2},j}}{\Delta x} + Q_{S}^{v} \frac{u_{i-\frac{1}{2},j} - u_{i-\frac{1}{2},j-1}}{\Delta y}$$

By rearranging (37), one has at the  $(i + \frac{1}{2}, j)$  node

$$u_{i+\frac{1}{2},j}^{n+1} = \frac{1}{H_{i+\frac{1}{2},j}^*} \left[ H_{i+\frac{1}{2},j}^n u_{i+\frac{1}{2},j}^n - \Delta t F_{i+1/2,j}^n - g \frac{\Delta t}{\Delta x} H_{i+\frac{1}{2},j}^n \left( \eta_{i+1,j}^{n+1} - \eta_{i,j}^{n+1} \right) \right]$$

$$\tag{40}$$

where

$$H_{i+1/2,j}^* = \frac{1}{H_{i+1/2,j}^n + \gamma_{i+\frac{1}{2},j} \Delta t}.$$

A semi-implicit finite difference scheme for the *y*-momentum equation at the *v*-node can be devised in a similar way. More specifically, at node (i, j + 1/2), one has

$$v_{i,j+\frac{1}{2}}^{n+1} = \frac{1}{H_{i,j+\frac{1}{2}}^*} \left[ H_{i,j+\frac{1}{2}}^n v_{i,j+\frac{1}{2}}^n - \Delta t G_{i,j+\frac{1}{2}}^n - g \frac{\Delta t}{\Delta x} H_{i,j+\frac{1}{2}}^n \left( \eta_{i,j+1}^{n+1} - \eta_{i,j}^{n+1} \right) \right]$$

$$(41)$$

where  $G_{i,j+1/2}^n$  represents the explicit discretization scheme of the advection.

The FD equations for the non-conservative momentum equations (33) and (34) are identical to (40) and (41) except for  $F^n$  and  $G^n$ . More

precisely, the following scheme

$$\begin{split} F_{i+\frac{1}{2},j}^{n} &= u_{i+\frac{1}{2},j} \left[ \frac{(C_{UU,E} - 1)Q_{E}^{u} - (C_{UU,W} - 1)Q_{W}^{u}}{\Delta x} \right. \\ &+ \frac{(C_{UV,N} - 1)Q_{N}^{v} - (C_{UV,S} - 1)Q_{S}^{v}}{\Delta y} \right] + \\ &C_{UU}u_{i+1/2,j}^{n} H_{i+1/2,j}^{n} \left[ \frac{\lambda_{x,-1}u_{i-1/2,j}^{n} + \lambda_{x,0}u_{i+1/2,j}^{n} + \lambda_{x,1}u_{i+3/2,j}^{n}}{\Delta x} \right] + \\ &C_{UV}v_{i+1/2,j}^{n} H_{i+1/2,j}^{n} \left[ \frac{\lambda_{y,-1}u_{i+1/2,j-1}^{n} + \lambda_{y,0}u_{i+1/2,j}^{n} + \lambda_{y,1}u_{i+1/2,j+1}^{n}}{\Delta y} \right], \end{split}$$

$$(42)$$

is considered in the discretization of the *x*-momentum equation. Here, the value of  $\lambda_{x,l}$  and  $\lambda_{y,l}$  depends on the upwind direction, more precisely,

$$\left\{ \begin{array}{ll} \lambda_{x,-1} = -1, \ \lambda_{x,0} = 1, \ \lambda_{x,1} = 0 & \text{for } u_{i+1/2,j} > 0 \\ \lambda_{x,-1} = 0, \ \lambda_{x,0} = -1, \ \lambda_{x,1} = 1 & \text{for } u_{i+1/2,j} < 0 \end{array} \right.$$

$$\left\{ \begin{array}{ll} \lambda_{y,-1} = -1, \ \lambda_{y,0} = 1, \ \lambda_{y,1} = 0 & \text{for } v_{i+1/2,j} > 0 \\ \lambda_{y,-1} = 0, \ \lambda_{y,0} = -1, \ \lambda_{y,1} = 1 & \text{for } v_{i+1/2,j} < 0 \end{array} \right.$$

Since  $v_{i+1/2,j}$  is not defined on the u-node where the x-momentum is discretized,  $v_{i+1/2,j}$  is interpolated from the surrounding v-nodes through

$$v_{i+1/2,j}^n = \frac{v_{i,j+1/2}^n + v_{i+1,j+1/2}^n + v_{i,j-1/2}^n + v_{i+1,j-1/2}^n}{4}$$

Note that  $G^n$  for the y-momentum equation (34) is defined in an analogous manner.

The discretization formulas (40) and (41) are defined at the wet edges and the velocity on the dry edges is assumed to be zeros (although this is not strictly true at the wetting/drying front).

## B.O.3. Solution algorithm

The solution  $\eta^{n+1}$ ,  $u^{n+1}$ ,  $v^{n+1}$  can be obtained either by (i) solving the system of nonlinear equations (35), (40), and (40) simultaneously or by (ii) solving a reduced system of equations arising from the substitution of (40), and (40) into (35) (Casulli, 2009). Such a reduced system of nonlinear algebraic equations is given by

$$\begin{split} V_{i,j}(\eta_{i,j}^{n+1}) - \mathcal{A}_{i+1/2,j}\eta_{i+1,j}^{n+1} - \mathcal{A}_{i-1/2,j}\eta_{i-1,j}^{n+1} + \mathcal{D}_{i,j}\eta_{i,j}^{n+1} - \mathcal{A}_{i,j+1/2}\eta_{i,j+1}^{n+1} \\ - \mathcal{A}_{i,j-1/2}\eta_{i,i-1}^{n+1} = V_{i,j}^n(\eta_{i,j}^n) - \mathcal{B}_{i+1/2,j} + \mathcal{B}_{i-1/2,j} - \mathcal{B}_{i,j+1/2} + \mathcal{B}_{i,j-1/2} \end{split}$$

wher

$$A_{i\pm 1/2,j} = g \frac{\Delta t^2}{\Delta x} \frac{H_{i\pm 1/2,j}^n}{H_{i\pm 1/2,j}^*} A_{i\pm 1/2,j}, \ A_{i,j\pm 1/2} = g \frac{\Delta t^2}{\Delta y} \frac{H_{i,j\pm 1/2}}{H_{i,j\pm 1/2}^*} A_{i,j\pm 1/2}$$

$$D_{i,j} = A_{i+1/2,j} + A_{i-1/2,j} + A_{i,j+1/2} + A_{i,j-1/2}$$

$$\begin{split} \mathcal{B}_{i\pm 1/2,j} &= \frac{\Delta t}{H^*_{i\pm 1/2,j}} A_{i\pm 1/2,j} \left[ H^n_{i\pm 1/2,j} u^n_{i\pm 1/2,j} - \Delta t F^n_{i\pm 1/2,j} \right] \\ \mathcal{B}_{i,j\pm 1/2} &= \frac{\Delta t}{H^*_{i,j\pm 1/2}} A_{i,j\pm 1/2} \left[ H^n_{i,j\pm 1/2} v^n_{i\pm 1/2,j} - \Delta t G^n_{i,j\pm 1/2} \right]. \end{split}$$

A more compact form of the above system of equations is

$$V(\eta) + T\eta = b \tag{43}$$

where  $\eta$  is a vector of the solution at the next time level  $\{\eta_{i,j}^{n+1}\}$ , **T** is the matrix with  $\mathcal{A}$  and  $\mathcal{D}$  as its entries, **V** is the vector of the water volume, and **b** is the known right hand side vector. Note that **T** is symmetric with positive diagonal entries and negative off-diagonal entries; it has at most five nonzero entries for each row (a five-point stencil).

The system of equations (43) is nonlinear and is solved by the Newton–Raphson method:

$$\boldsymbol{\zeta}^{m+1} = \boldsymbol{\zeta}^m - \mathbf{J}^{-1}[\mathbf{V}(\boldsymbol{\zeta}^m) + \mathbf{T}\boldsymbol{\zeta}^m - \mathbf{b}]$$
(44)

where m is the iteration step, and  $J(\zeta^m)$  is the Jacobian matrix of (43) evaluated at  $\zeta^m$ . A good approximation of the Jacobian is

$$\mathbf{J} = \mathbf{P}(\boldsymbol{\eta}^m) + \mathbf{T} \tag{45}$$

where **P** is a diagonal matrix of the wet area of the cell  $\Delta x \Delta y \phi$  (Casulli, 2009). The formula (44) is iterated, with the solution at the current time step as an initial guess  $\eta^0 = \zeta^n$ , until a criterion  $|\zeta^{m+1} - \zeta^m| < tol$  is met and set  $\eta^{n+1} = \zeta^m$ . Subsequently, the velocities at the time level n+1 are obtained from (40) and (41) with the now known  $\zeta^{n+1}$ .

#### References

- Anon., NOAA tide and currents, https://tidesandcurrents.noaa.gov/.
- Anon., 2015. North Atlantic Coast Comprehensive Study: Resilient Adpatation to Increasing Risk, Main report, US Army Corps of Engineers.
- Bunya, S., Dietrich, J., Westerink, J., Ebersole, B., Smith, J., Atkinson, J., Jensen, R., Resio, D., Luettich, R., Dawson, C., Cardone, V., Cox, A., Powell, M., Westerink, H., Roberts., H., 2010. A high resolution coupled riverine, tide, wind, wind wave, and storm surge model for southern Louisiana and Mississippi: Part I model development and validation. Mon. Weather Rev. 138, 345–377.
- Casulli, V., 1990. Semi-implicit finite difference methods for the two-dimensional shallow water equations. J. Comput. Phys. 86 (1), 56–74.
- Casulli, V., 2009. A high-resolution wetting and drying algorithm for free-surface hydrodynamics. Internat. J. Numer. Methods Fluids 60 (4), 391–408. http://dx. doi.org/10.1002/fld.1896.
- Casulli, V., 2019. Computational grid, subgrid, and pixels. Internat. J. Numer. Methods Fluids 1–16. http://dx.doi.org/10.1002/fld.4715.
- Casulli, V., Stelling, G.S., 2011. Semi-implicit subgrid modelling of three-dimensional free-surface flows. Internat. J. Numer. Methods Fluids 67 (4), 441–449. http://dx.doi.org/10.1002/fld.2361.
- D'Alpaos, L., Defina, A., 2007. Mathematical modeling of tidal hydrodynamics in shallow lagoons: A review of open issues and applications to the venice lagoon. Comput. Geosci. 33, 476–496.

- Danielson, J.J., Poppenga, S.K., Tyler, D.J., Palaseanu-Lovejoy, M., Gesch, D.B., 2018.
  Coastal National Elevation Database. U.S. Geological Survey Fact Sheet 2018-3037, <a href="http://dx.doi.org/10.3133/2018">http://dx.doi.org/10.3133/2018</a>.
- Defina, A., 2000. Two-dimensional shallow flow equations for partially dry areas. Water Resour. Res. 36 (11), 3251–3264. http://dx.doi.org/10.1029/2000WR900167.
- Dietrich, J.C., Bunya, S., Westerink, J.J., Ebersole, B.A., Smith, J.M., Atkinson, J.H., Jensen, R., Resio, D.T., Luettich, R.A., Dawson, C., Cardone, V.J., Cox, A.T., Powell, M.D., Westerink, H.J., Roberts, H.J., 2010. A high resolution coupled riverine, tide, wind, wind wave, and storm surge model for southern Louisiana and Mississippi: Part II: synoptic description and analyses of Hurricanes Katrina and Rita. Mon. Weather Rev. 138, 378–404.
- Hope, M.E., Westerink, J.J., Kennedy, A.B., Kerr, P.C., Dietrich, J.C., Dawson, C., Bender, C.J., Smith, J.M., Jensen, R.E., Zijlema, M., et al., 2013. Hindcast and validation of Hurricane Ike (2008) waves, forerunner, and storm surge. J. Geophys. Res. Ocean. 118 (9), 4424–4460.
- Kerr, P.C., Donahue, A.S., Westerink, J.J., Luettich Jr., R.A., Zheng, L.Y., Weisberg, R.H., Huang, Y., Wang, H.V., Teng, Y., Forrest, D.R., Roland, A., Haase, A.T., Kramer, A.W., Taylor, A.A., Rhome, J.R., Feyen, J.C., Signell, R.P., Hanson, J.L., Hope, M.E., Estes, R.M., Dominguez, R.A., Dunbar, R.P., Semeraro, L.N., Westerink, H.J., Kennedy, A.B., Smith, J.M., Powell, M.D., Cardone, V.J., Cox, A.T., 2013. U.S. IOOS coastal and ocean modeling testbed: Inter-model evaluation of tides, waves, and hurricane surge in the Gulf of Mexico. J. Geophys. Res. Ocean. 118 (10), 5129–5172.
- Sehili, A., Lang, G., Lippert, C., 2014. High-resolution subgrid models: background, grid generation, and implementation. Ocean Dyn. 64, 519–535. http://dx.doi.org/10.1007/s10236-014-0693-x.
- Stelling, G., Duinmeijer, S., 2003. A staggered conservative scheme for every Froude number in rapidly varied shallow water flows. 1354, 1329–1354.
- Tanaka, S., Bunya, S., Westerink, J., Dawson, C., Luettich, R., 2011. Scalability of an unstructured grid continuous Galerkin based hurricane storm surge model. J. Sci. Comput. 46, 329–358.
- Te Chow, V., 1982. Open Channel Hydraulics. McGraw-Hill International Book Company.
- Viero, D.P., 2019. Modelling urban floods using a finite element staggered scheme with an anisotropic dual porosity model. J. Hydrol. 568, 247–259.
- Viero, D.P., Valipour, M., 2017. Modeling anisotropy in free-surface overland and shallow inundation flows. Adv. Water Resour. 104, 1–14.
- Volp, N., van Prooijen, B., Pietrzak, J., Stelling, G., 2016. A subgrid based approach for morphodynamic modelling. Adv. Water Resour. 93, 105–117. http://dx.doi.org/10. 1016/j.advwatres.2015.07.013, Numerical modelling of river morphodynamics.
- Volp, N.D., van Prooijen, B.C., Stelling, G.S., 2013. A finite volume approach for shallow water flow accounting for high-resolution bathymetry and roughness data. Water Resour. Res. 49 (7), 4126–4135. http://dx.doi.org/10.1002/wrcr.20324.
- Whitaker, S., 1999. The method of volume averaging. http://dx.doi.org/10.1007/978-94-017-1114-2, URL http://www.springer.com/series/6612.
- Wu, G., Li, H., Liang, B., Shi, F., Kirby, J.T., Mieras, R., 2017. Subgrid modeling of salt marsh hydrodynamics with effects of vegetation and vegetation zonation. Earth Surf. Process. Landf. 42 (12), 1755–1768. http://dx.doi.org/10.1002/esp.4121.
- Wu, G., Shi, F., Kirby, J.T., Mieras, R., Liang, B., Li, H., Shi, J., 2016. A pre-storage, subgrid model for simulating flooding and draining processes in salt marshes. Coast. Eng. 108, 65–78. http://dx.doi.org/10.1016/j.coastaleng.2015.11.008, URL http://www.sciencedirect.com/science/article/pii/S0378383915001969.
- Zachry, B., Booth, W., Rhome, J., Sharon, T., 2017. A national view of storm surge risk and inundation. Weather Clim. Soc. 7, 109-117.